A STUDY OF SHRINKAGE CRACK PATTERNS

KELLY A. LINEHAN

A STUDY OF SHRINKAGE CRACK PATTERNS

by

Kelly A. Linehan, B.Sc.(Hons.)

A THESIS SUBMITTED TO THE
SCHOOL OF GRADUATE STUDIES
IN PARTIAL FULFILLMENT
OF THE REQUIREMENTS
FOR THE DEGREE OF
MASTER OF SCIENCE

DEPARTMENT OF PHYSICS AND PHYSICAL OCEANOGRAPHY
MEMORIAL UNIVERSITY OF NEWFOUNDLAND
MAY 1997

ST. JOHN'S NEWFOUNDLAND

Abstract

Shrinkage crack patterns which develop in a layer of a drying slurry of Al_2O_3 powder and water are studied. The ways in which the pattern changes with the depth of the layer, with friction between the layer and the container, and with added impurities are described. A statistical analysis is given of how changes in these experimental conditions affect the lengthscale of the pattern, the junction angles between cracks, the nucleation sites of the cracks, and the number of sides of the polygons formed by the cracking process. The lengthscale of the pattern increases linearly with depth. Longer lengthscales are observed in patterns where the friction between the layer and its substrate is reduced which shows that friction is the main source of stress for fracture. Most crack junctions are perpendicular showing that crack junctions are formed primarily through intersections of new cracks with pre-existing ones. These results are compared with the recent results of Groisman and Kaplan.

Acknowledgements

I am grateful to my supervisor and collaborator, Dr. John de Bruyn, for his advice and support throughout my program. For their help with the apparatus, developing the pictures, and helpful discussions about the work, I thank Bill Kieley, Anna Crawford, Wayne Holly, John Power, Bob Bradley, Roger Guest, Rick Power, Steve Morris, and Nicolas Rivier. I gratefully acknowledge the financial support of Memorial University of Newfoundland and NSERC. For his inexhaustible strength, support, and good humour, I thank Steve Short.

Contents

List of Figures

List of Tables

Chapter 1
Introduction

Shrinkage crack patterns are commonly observed in many naturally occurring systems [1]. The patterns are complicated arrays of polygons formed by many intersecting cracks. Some two-dimensional examples include cracks in the glaze on a ceramic mug, dried mud, or dried paint. Fig. 1.1 is a picture of cracks in a layer of dried mud of approximate area 20 cm by 20 cm. In some cases the crack pattern propagates in the third direction. Examples are the long hexagonal columns which form in cooling basalt flows, like the Giant's Causeway shown in Fig. 1.2, and ice-wedge polygons in permafrost [2] in the Arctic. The lengthscales of these patterns range from a few millimetres in the glaze in ceramics to 30 metres in the ice-wedge polygons. The cracks in two-dimensional patterns may be classified as diffuse or brittle. Diffuse cracks are rough and jagged, like the cracks in Fig. 1.1, while brittle cracks have smooth faces and are found in substances like ceramics.

The study of fracture has been subject to a renewed interest since the landmark paper by Griffith in 1920 [3]. Geologists have long been interested in fracture patterns because understanding their formation may give information on the environmental conditions, like temperatures and salinity of water, of previous eras [4]. Fracture is important in industrial applications concerning coatings and the changes in strengths of materials which have surface scratches. Crack patterns are also of interest in the field of nonlinear dynamics because the dynamics of fracture are not well understood, and

crack patterns are an example of irreversible pattern formation.

Figure 1.1: Cracks in a dried mud layer in Chile. The area shown is approximately 20 cm by 20 cm. Photograph by Stephen Short, June, 1996.

1.1 Review of Previous Work

Shrinkage crack patterns arise in materials which contract while cooling or drying. This work considers two-dimensional shrinkage crack patterns formed as a result of drying. As a layer of a material dries, its volume decreases as the water evaporates, and the layer contracts. Due to adhesion to the substrate, stress builds in the layer, and when the stress exceeds the local tensile strength, the material fractures. When the resulting crack opens, the stress is relieved locally along the sides of the crack, but becomes concentrated at

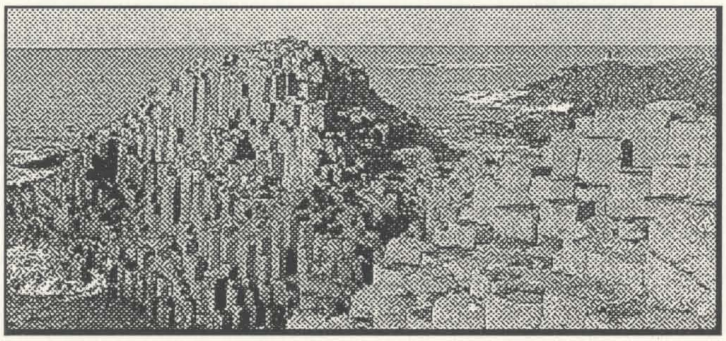

Figure 1.2: The Giant's Causeway in Northern Ireland. Copyright 1995, interKnowledge Corp.

the crack tip. As a result the crack propagates lengthwise until the stress at the tip is reduced to below the local strength of the material [5]. In a homogeneous medium the crack will form and grow perpendicular to the direction of maximum stress so as to relieve the stress most efficiently.

A crack pattern forms as multiple cracks grow and intersect. The stress in the vicinity of a crack face is parallel to the face since a free surface can support no stress. Thus any crack nucleating at or growing to meet the edge of a preexisting crack will meet that crack perpendicularly. Although two independent cracks will meet at a 90° junction angle, 120° junction angles have also been observed. Non-perpendicular junctions are formed by other methods of crack junction formation which include the splitting of a crack tip into two or more cracks, the joining of two initially parallel cracks propagating together to form a single crack, or the nucleation of multiple cracks at some nucleation site. Nucleation sites are impurities in the material

such as air bubbles, sand grains, dust, or microscopic inhomogeneities such as microscopic defects in the material.

It has been proposed that in a homogeneous material under uniform contraction, 120° junction angles give the largest ratio of elastic energy relief to the energy of new surfaces being created by cracking [6]. While the presence of 120° junction angles has been noted in thin layers of various materials [4, 7, 9] and in computer models of fracture [9], it has been noticed by several authors that most crack junctions in two-dimensional patterns are at 90° [1, 7, 10, 11].

Two-dimensional shrinkage crack patterns in mud in ancient geological formations have been discussed [6, 10, 11, 12]. Crack patterns in mud in containers left in the sun to dry were studied qualitatively [4, 10, 12] and it was observed that larger polygons were found in thicker layers and in more rapidly dried layers. Most crack junctions were found to be orthogonal [10, 11] but a number of 120° junction angles were found in the thinnest layers [4].

Lachenbruch studied contraction crack patterns in the ice-wedge polygons in the permafrost in the Arctic, which are similar to mud crack patterns [2]. Ice-wedge polygons formed, over the course of hundreds of years, after fractures opened in the layer of permafrost due to thermal tension. In the spring thaws, the top layer of ice melted and water ran into the cracks. During the winter months, the water froze and expanded, making the cracks wider. Many fractures formed and interacted, creating the ice-wedge polygonal pat-

tern observed in the Arctic. Lachenbruch provides a model of a stress relief zone in the vicinity of a single fracture. The stress at a crack wall is zero. Far away from the crack the stress in the bulk is equal to the pre-cracking stress, so there exists a zone of stress relief near a crack. The width of the zone depends strongly on depth of the crack as well as on the stress distribution in the layer at a given crack depth. The model indicates that the spacing between the cracks is the same order of magnitude as the crack depth.

Skjeltorp and Meakin [9] studied crack patterns which formed in a monolayer of polystyrene microspheres dried between two glass plates. At early stages of growth, they observed the cracks to be linear with rapid growth. Most crack junction angles were 120° due to the hexagonal packing of the microspheres. At later stages, the growth slowed and the shapes of the cracks became irregular. They presented a two-dimensional computer model of fracture where the layer was represented by a triangular network of nodes and bonds which initially formed a triangular lattice. Each node was bonded to its six nearest neighbours and more weakly to an underlying substrate, with the total system energy given by the harmonic approximation. The lattice was initially stretched isotropically, then a bond was selected at random, and broken with a probability which depended on the energy between nodes. The lattice was then allowed to relax, and the process repeated. The resulting pattern of cracks was similar to the experimental pattern.

Hornig *et al.* [13] presented a similar spring-block model with a triangular lattice and harmonic bonds between nodes and the substrate. The stress

in the layer was increased by isotropically stretching the substrate. The forces acting on the springs were calculated and where the force exceeded the breakdown threshold, chosen by a given probability distribution in the range $[f_{min}, f_{min} + W]$, the springs were removed. The parameter W/f_{min} characterized the disorder in the system. They found a transition from irregular to regular cracks as the the strength of disorder decreased, and found a power law dependence of the mean fragment size of the polygons on the strain.

Leung and Andersen [14] used a spring-block model of blocks in a square array connected to nearest neighbours with springs and in contact with an underlying substrate with lattice constant a. The drying process was simulated by fixing a and the relaxed spring length to impose an initial tensile strain s while increasing the spring constant to increase stiffness. Force on the blocks was calculated and the stress was relieved through spring breaks or block slips with threshold dynamics: If the force on a block exceeded the slipping threshold F_s, the block slipped to a force-free position, if the force exceeded the breaking threshold $F_c = \kappa F_s$ the spring broke. The parameter κ defined the characteristics of the system: larger κ represented a stronger material or weaker substrate coupling. For a large enough s, they found a phase transition in the crack morphology from small and randomly located for smaller κ to larger and more ordered for larger κ. They found a transition in the probability density of fragment area, from log-normal to a possible power law dependence, as κ increased. This implies that as the friction is

reduced or the material made stronger, the distribution of fragment sizes changes from random to more ordered.

A similar spring-block model was used by Andersen *et al.* [15]. Blocks on a square array were connected by springs to their nearest neighbours and also connected to a substrate. The same threshold dynamics as above were used. They noticed that for large κ the crack junctions were perpendicular, while for smaller κ a wider range of junction angles was present, where large κ represented a stronger material or reduced bottom friction.

Groisman and Kaplan [7] studied shrinkage crack patterns in experiments similar to this work. They allowed coffee-water mixtures to dry on circular glass plates, 14 cm in diameter, or on square boxes ranging from 20 cm $\times$ 20 cm to 48 cm $\times$ 48 cm. They found a linear relationship between the scale of the pattern and the thickness of the dried layers, which ranged from 2 mm to 16 mm. They examined the effect of bottom friction by drying layers of similar thickness on an untreated glass plate, a plate coated with 2 mm of grease, and a plated coated with 6 mm of vaseline. They observed the most cracks in the untreated plate and the fewest in the vaseline coated plate, which showed that reducing the bottom friction increases the lengthscale of the pattern. They measured the percentage of 120° junction angles as a function of depth and observed a transition from almost zero in thicker layers to about 30% in layers thinner than 4 mm. They also noticed a transition in the pattern morphology at this thickness. Above this thickness the cracks formed a polygonal network and the crack edges were smoother,

while for layers less than 4 mm thick there was no definite polygonal network and the cracks were diffuse. The transition in morphology was attributed to facilitated nucleation from inherent inhomogeneities which caused many cracks to form at the same time and screen each other. They suggested that 120° junction angles occur when a crack tip splits. For thinner layers, this occurs at defects in the material. The transition to an increased number of 120° junctions shows that another lengthscale associated with the texture of the material is important during cracking. A similar transition was also observed in drying cornflour-water mixtures by Webb and Beddoe [8].

A three-dimensional crack pattern is created when a two-dimensional crack pattern propagates in the third dimension as a result of a cooling or drying gradient. The gradient causes tension in the material since the cooler or drier portion will be contracted relative to the warmer or wetter portion. Examples occur in basaltic lava flows, like the Giant's Causeway shown in Fig. 1.2, in which a cooling front propagated from top to bottom as the hot rock cooled. The stress was relieved by cracking in the form of long, thin hexagonal columns. The cracking in the third dimension has been modeled in experiments by subjecting a thin layer of a material to a drying or cooling front in the plane of the layer.

Yuse and Sano [16] examined the morphology of single cracks which formed in glass plates with a moving thermal gradient. The crack motion exhibited a transition from straight to oscillatory to branched as the speed of the cooling front increased. The transition was a result of an instability in the crack tip.

Marder [17] observed that the crack motion in these experiments could be studied with the methods of nonlinear dynamics.

Fracture patterns in thin layers of a directionally dried colloidal suspension between two glass plates have been studied by Allain and Limat [18]. The suspension was allowed to dry through one open edge and the resultant pattern of cracks was regularly spaced. In an analysis of this work, Komatsu and Sasa [19], explained the regular spacing of the cracks in terms of maximum stress relief: The first crack formed where there was maximum stress, *i.e.*, the middle of the sample, the next cracks were in the middle of the two segments, and this process repeated until all the water was evaporated.

Morris *et al.* [20] observed patterns which formed in directionally dried layers of Aluminum Oxide (Al_2O_3) and water in a 12 cm by 8 cm cell. The layer cracked in long thin strips perpendicular to the drying front. They studied the effects of bottom friction by drying layers on various substrates, including sandpaper, polished stainless steel, and mercury. They found that the lengthscale of the pattern depended on layer thickness only when there was sufficiently large friction between the layer and its substrate.

1.2 Outline of This Project

In this project we provide a quantitative analysis of two-dimensional shrinkage crack patterns formed under various experimental conditions. The experimental parameters are layer depth, friction between the layer and the substrate, and added impurities. We determine the mean lengthscale of the pattern as a function of depth, and examine how the lengthscale changes

when friction between the layer and its substrate is reduced and when impurities are added to the layer before drying. The results of Groisman and Kaplan [7] indicate that there is a linear relationship between the length-scale of the pattern and the thickness of the dried layer, but do not show quantitatively how the slope depends on friction between the layer and its substrate or with the level of impurities in the layer. We find the average area per polygon and expect it to scale linearly with depth squared as shown in the results of Groisman and Kaplan. By measuring the crack junction angles and counting the number of sides per polygon we obtain quantitative information about the distribution of crack junction angles. The distribution is expected to have a strong peak at 90° in thick layers and for thinner layers, a transition to increased numbers of 120° is expected [7, 8]. We examine the distribution of crack junction angles and changes in the distribution as a function of the experimental parameters. With Fourier analysis, we study the statistical properties of the crack patterns which give information about the spatial structure of the pattern and are useful in classifying the patterns.

Chapter 2
Experimental

2.1 Apparatus

A schematic illustration of the apparatus used is shown in Figure 2.1. To maintain a stable environment and constant drying rate, the experiments were conducted inside an insulated enclosure. The enclosure was made from 1.1 cm plywood and had outside dimensions of 76 cm × 76 cm × 244 cm. It was insulated with 5.1 cm styrofoam insulation lining the inside. Four fifteen watt light bulbs installed at the top of the insulated enclosure were used as the heat source for the experiments, and also illuminated the mud layer for video recordings made during the cracking process. The temperature at the layer was maintained between 25°C and 28°C for all runs, and was constant to within 1°C during a given run. A thin sheet of translucent plastic was placed below the bulbs to diffuse the light, producing more even illumination. A charge-coupled device video camera was positioned near the top of the housing and was used with a GYYR time lapse video recorder, model number TLC1800R, to record the cracking process.

Individual frames from the video record were digitized for analysis using an Imaging Technology Inc. PC/vision-plus frame grabber card in a personal computer. The frame grabber captured images of 480 × 512 pixels where the intensity of each pixel was stored as an 8-bit binary number, *i.e.*, the digitized intensity range was from 0 to 255. A light table beneath the mud

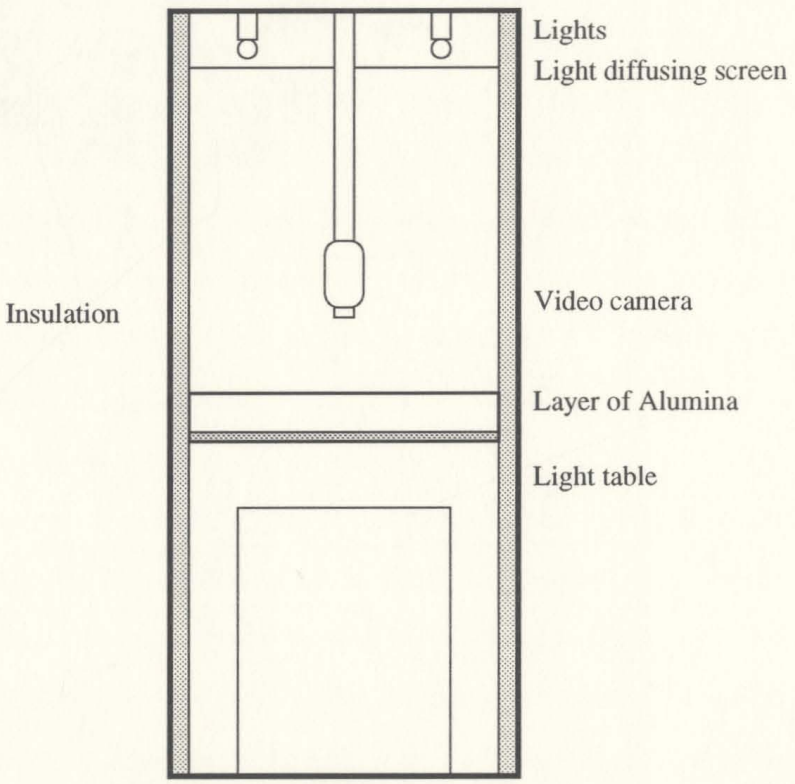

Figure 2.1: The experimental apparatus.

layer provided illumination from below for photographs taken at the end of each run. The photographs and digitized images were used for the data analysis.

2.2 Experimental Conditions

The "mud" used was a slurry of water and Aluminum Oxide C (chemical formula Al_2O_3) powder supplied by Degussa Canada Ltd. The Al_2O_3 or alumina particles are 130 Å in size and insoluble in water. The slurry was poured into a 62.2 cm × 62.2 cm Plexiglas pan with a sturdy 2.5 cm thick base and allowed to dry for 5 – 17 days depending on the thickness of the layer. Between 60.1 g to over 500 g of alumina was mixed with 1 – 3 l of water using a hand blender.

The experimental conditions varied were the thickness of the layer, the friction between the layer and its substrate, and impurities added to the slurry. For the runs referred to as Type A experiments, the alumina was used with no added impurities, and the Plexiglas substrate was untreated. In the Tpye B experiments, the friction between the layer and the substrate was reduced by spraying the pan with a thin, transparent coating of teflon (Crown 66075 dry film lubricant). There were no impurities added to the Type B experiments. The Type C experiments also had bottom friction reduced by a teflon coating, but impurities were introduced by sprinkling 10 cm^3 of sand grains, 425 – 500 μm in size, evenly over the top of the slurry before the drying began. These particles are $\sim 10^4$ times the size of the Al_2O_3 particles and on the same size scale as the layer thickness. The sand floated

on top of the layers. We did four runs of each type of experiment; the type of experiment, range of depths of the dried layer, mass M of Al_2O_3 used, volume V of water used, and approximate drying times t of each one is listed in Table 1. The depths listed are the ranges of depths of 8 cm squares within the container. The depth measurement is an average over 5 points within the sample area and the error in depth is the standard deviation of those five points. The squares were not physically divided, but distinguished by a grid drawn on the bottom of the pan. Over any given run, the depth of the sample areas varied by up to 2.2 mm which could be due to the supporting light table not being perfectly level or to the bottom plate being warped.

Type	layer depth (mm)	M (g)	V (l)	t (hr)
A	0.13 ± 0.02 — 0.63 ± 0.06	60.5± 1.0	1	95
A	0.40 ± 0.02 — 1.16 ± 0.05	116.7± 1.0	1	62
A	0.51 ± 0.02 — 1.41 ± 0.10	155.2± 1.0	1	108
A	1.73 ± 0.02 — 3.35 ± 0.21	495± 50	2.8	202
B	0.22 ± 0.02 — 0.80 ± 0.05	69.8± 1.0	1	120
B	0.32 ± 0.02 — 1.18 ± 0.09	116.1± 1.0	1	54
B	0.45 ± 0.02 — 1.51 ± 0.06	154.6± 1.0	1	122
B	1.91 ± 0.04 — 4.12 ± 0.46	500± 50	3	379
C	0.15 ± 0.02 — 0.62 ± 0.06	60.1± 1.0	1	100
C	0.32 ± 0.03 — 1.48 ± 0.06	138.4± 1.0	1	107
C	0.76 ± 0.05 — 1.84 ± 0.05	266.1± 1.0	1	90
C	1.76 ± 0.05 — 3.02 ± 0.12	450.7± 1.0	2	184

Table 1: Range of depths, mass M of Al_2O_3 used, volume V of water used, and approximate drying times t for the experimental runs.

Chapter 3
Results and Analysis

3.1 Qualitative Description of Patterns

The fracture patterns which form in all of the experimental runs have qualitative similarities. Fig. 3.1 is a picture of one of the patterns. The fractures which form first in the drying slurry are referred to as primary cracks. These cracks are typically an order of magnitude longer than the final lengthscale of the pattern. The faces of the cracks are smooth and there are no sharp bends except in the thinnest layers of Type C experiments. As the slurry dries further, successive generations of cracks open between the primary cracks forming a complicated pattern of polygons. The resulting pattern has a characteristic length scale. The polygons formed by the primary cracks and the following generations of cracks are predominantly four-sided. Most of the junctions between cracks are at right angles, with a few non-perpendicular junctions. Under all experimental conditions, the lengthscale of the pattern and area of the polygons increases with increasing layer depth.

There are also qualitative differences in the fracture patterns depending on the experimental conditions. For very thin layers in Type B experiments, the edges of the polygons tend to curl downwards because they do not stick to the surface. This curling does not occur for the other experimental conditions. For similar layer depths, the polygons in the Type B experiments have greater area than the polygons in Type A or Type C experiments.

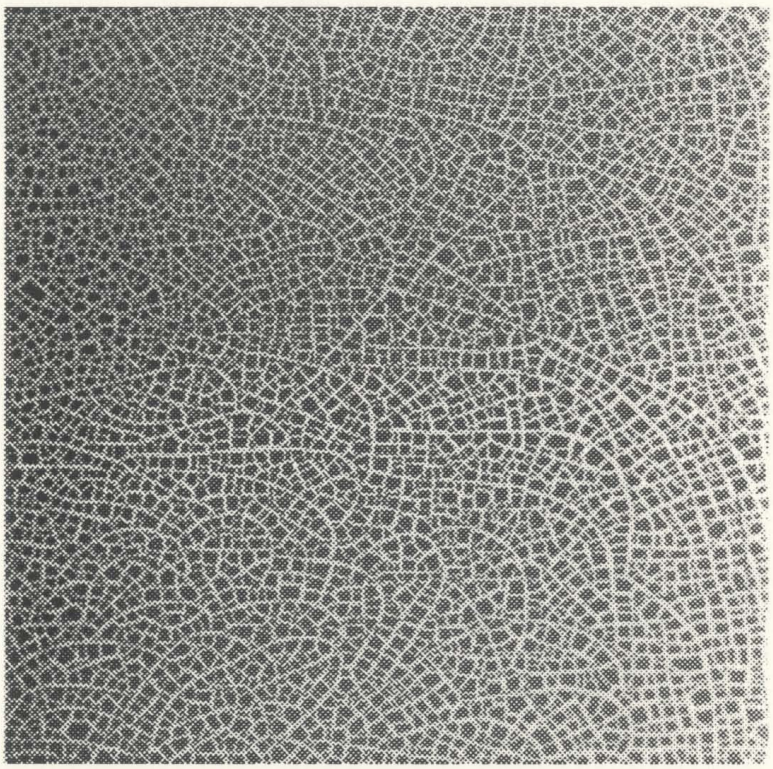

Figure 3.1: Pattern formed in a Type A experiment of approximately 16 cm by 16 cm in real space. $d = 0.57 \pm 0.02$ mm

3.2 Wavelength of the Pattern

We define the wavelength λ of the pattern as the average distance between cracks, and approximate it by $l/\sqrt{N_p}$ where N_p is the number of polygons in the sample area and l^2 is the area of the sample. The approximation would be an equality if all the polygons were equal sized squares. In this analysis l^2 was taken as a sample region of area 64.0 cm^2, well away from the edges of the container. The total area of the container is 3700 cm^2.

The wavelength as a function of depth d for each type of experiment is plotted in Figure 3.2. In all experiments, the wavelength increases linearly with depth. The error bars on λ in Fig. 3.2 are the same size as the symbols and are due to uncertainties in N_p and in the approximation itself. The scatter in the data increases for depths greater than about 2.75 mm, particularly in Fig. 3.2(b). This may be a result of the decreased effect of bottom friction with thickening layers, or of three-dimensional effects.

Lachenbruch's theory of ice wedge polygons [2] explains the effect of increasing lengthscale with increasing depth with a theory of stress relief. No normal stress can be maintained along the edge of a crack because it is a free surface. In the vicinity of the crack, the stress is reduced below the strength of the material. Further away, however, the stress builds until it exceeds the material's strength and another crack opens. The location of the new crack will depend to some extent on the range of the zone of stress relief. Lachenbruch [2] shows that the width of the zone of stress relief increases with the depth of the crack. Groisman and Kaplan [7] propose that since friction is

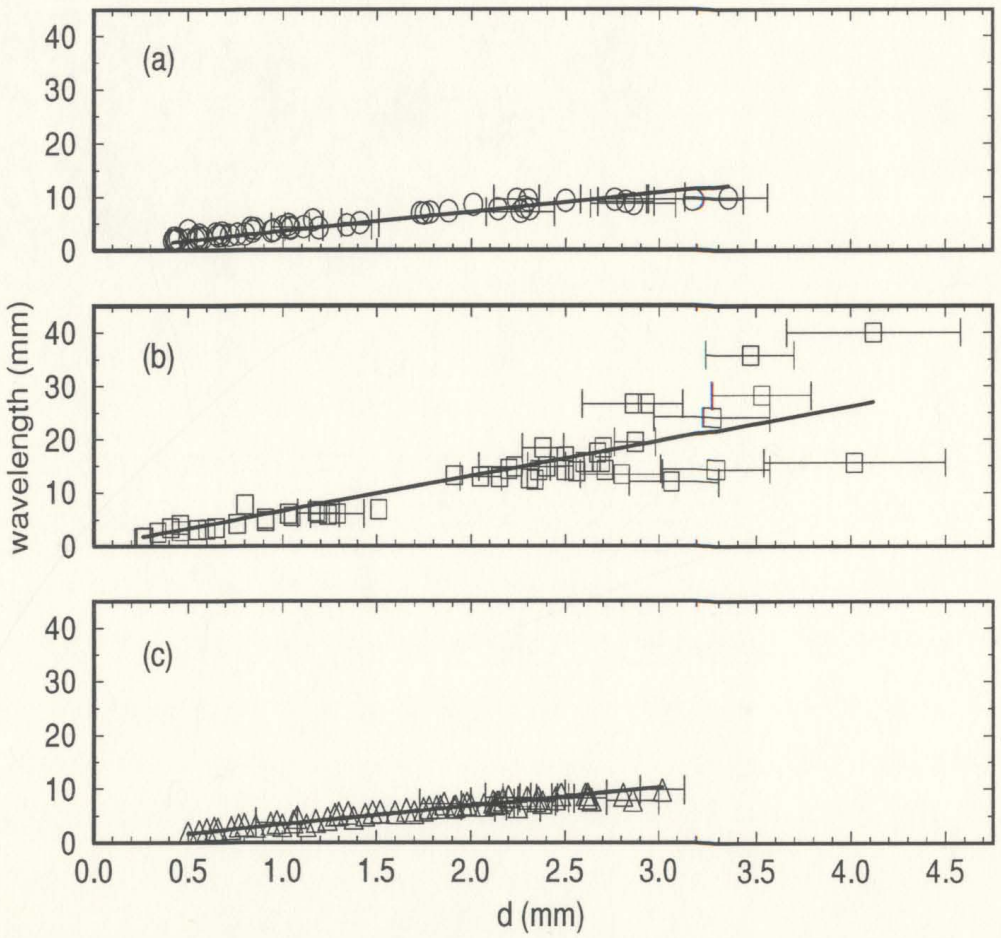

Figure 3.2: λ as a function of d with linear fits forced through the origin. (a) Type A experiments; $\lambda = (3.60 \pm 0.08)d$, (b) Type B experiments; $\lambda = (6.56 \pm 0.26)d$, (c) Type C experiments; $\lambda = (3.43 \pm 0.04)d$. Except where indicated otherwise, the error bars are approximately the same size as the symbols.

approximately proportional to the linear dimension of the polygon l, then the stress σ is approximately given by $F/d \propto l/d$ so that $l \propto \sigma_{cr} d$ where σ_{cr} is the critical stress required for cracking. This argument also indicates that the lengthscale of the pattern should increase linearly with depth.

The friction between the layer and the substrate was the main source of stress driving the fracture. The effects of reducing friction between the layer and substrate and increasing the impurities in a sample are seen in Fig. 3.2. Type A and Type B experiments had no added impurities so the layers had the same strength for fixed depth. Type B experiments had reduced bottom friction and so the layers were subject to less stress than the Type A layers. Because of the reduced stress in the Type B layers there were fewer fractures than in the Type A experiments at the same depths.

The largest impurities in all experiments were air bubbles which were formed when the slurry was poured into the container. On average, the air bubbles were 2 mm in diameter and there were estimated to be roughly 250 over the whole area in each experiment. Other impurities which were smaller but may also be significant were dust and microscopic cracks in the Al_2O_3. Impurities weakened the strength of the layer locally. The extent to which the Al_2O_3 was weakened depended on the relative size of the impurity: An impurity of the same size as the layer would have a greater effect than an impurity many times smaller than the layer thickness.

The Type B and Type C experiments had the same bottom friction. The added impurities in the Type C experiments reduced the strength of the

layers and as a result there were more fractures in these runs than the Type B experiments for the same depths.

The Type A and Type C experiments had similar lengthscales with depth while the Type B experiments had longer lengthscales. This suggests that the effects of reducing bottom friction and reducing strength with the introduction of impurities roughly cancel in this particular case.

3.3 Average Area of the Polygons

Using the mathematical package, Matlab, we converted the greyscale digitized images to black and white where a black pixel was part of a polygon and a white pixel was not. The threshold was chosen by inspection of the intensity values of the greyscale image. We divided the number of black pixels by the total number of pixels to get the fraction of the image that was solid, m. Figs. 3.3 – 3.11 are greyscale and black and white images from runs of varying depths from each type of experiment. Each image is 8 cm square in real space. In Fig. 3.12 we have plotted m as a function of depth for each set of experiments. It is constant with depth and has the same value for all runs within the experimental scatter. The average value of m over all experiments is $m = 0.557 \pm 0.015$. This implies that the fractional shrinkage in the area does not change with the varying experimental conditions.

Knowing the number of polygons N_p in the sample area, we calculated the average area per polygon A_p which is related to the wavelength of the

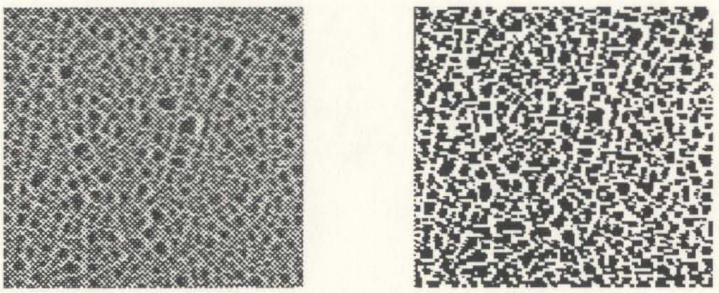

Figure 3.3: Greyscale and black and white images of an 8 cm $\times$ 8 cm region of the crack pattern for a Type A experiment with $d = 0.54 \pm 0.02$ mm.

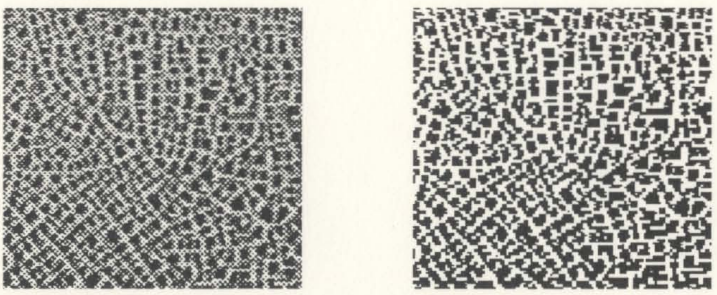

Figure 3.4: Greyscale and black and white images of an 8 cm $\times$ 8 cm region of the crack pattern for a Type A experiment with $d = 0.66 \pm 0.02$ mm.

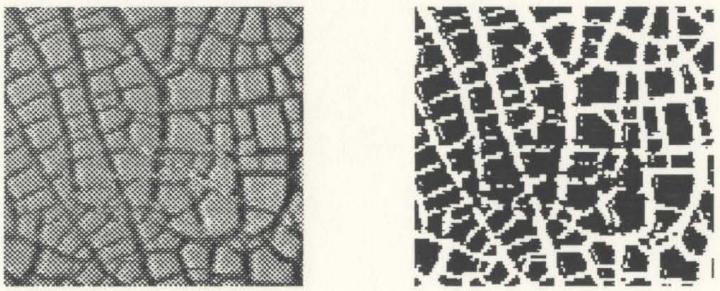

Figure 3.5: Greyscale and black and white images of an 8 cm $\times$ 8 cm region of the crack pattern for a Type A experiment with $d = 1.78 \pm 0.03$ mm.

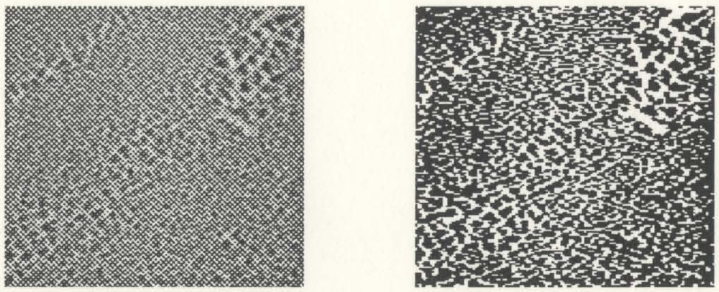

Figure 3.6: Greyscale and black and white images of an 8 cm $\times$ 8 cm region of the crack pattern for a Type B experiment with $d = 0.26 \pm 0.02$ mm.

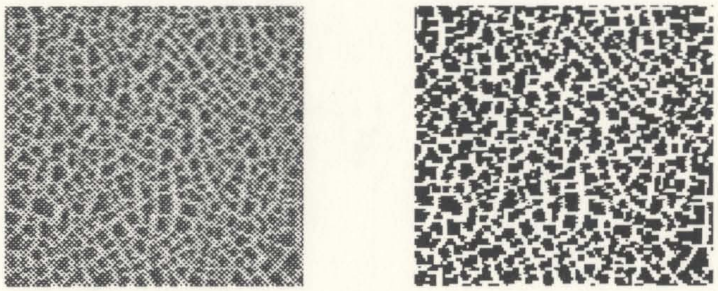

Figure 3.7: Greyscale and black and white images of an 8 cm $\times$ 8 cm region of the crack pattern for a Type B experiment with $d = 0.58 \pm 0.02$ mm.

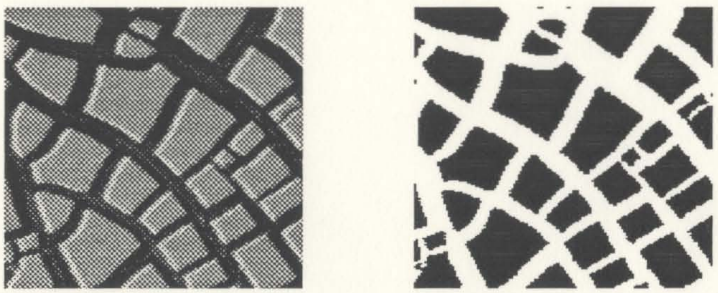

Figure 3.8: Greyscale and black and white images of an 8 cm $\times$ 8 cm region of the crack pattern for a Type B experiment with $d = 2.64 \pm 0.09$ mm.

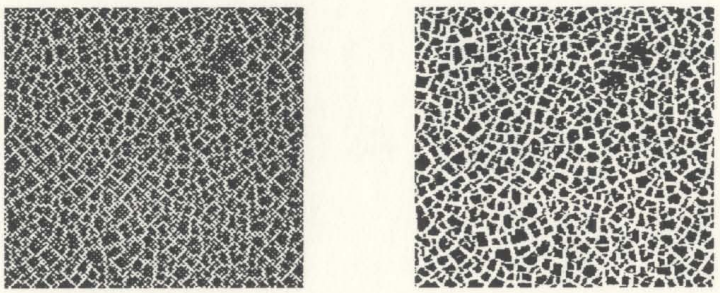

Figure 3.9: Greyscale and black and white images of an 8 cm × 8 cm region of the crack pattern for a Type C experiment with $d = 0.60 \pm 0.02$ mm.

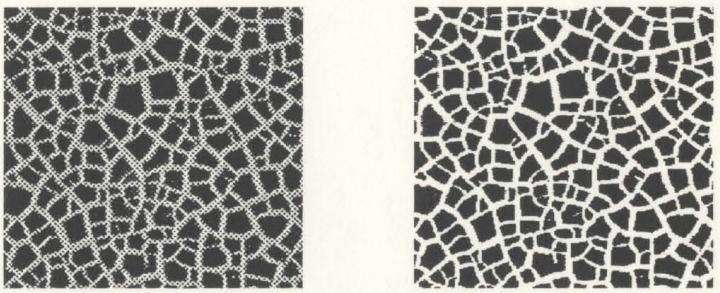

Figure 3.10: Greyscale and black and white images of an 8 cm × 8 cm region of the crack pattern for a Type C experiment with $d = 1.23 \pm 0.03$ mm.

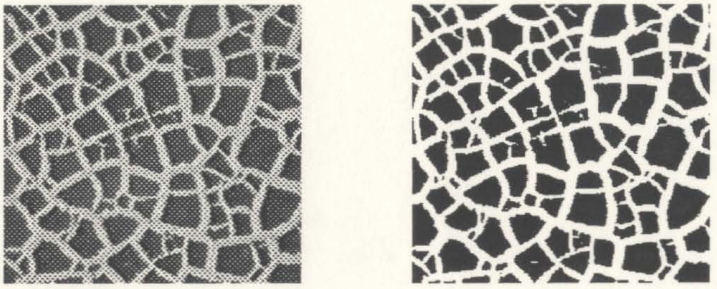

Figure 3.11: Greyscale and black and white images of an 8 cm × 8 cm region of the crack pattern for a Type C experiment with $d = 2.13 \pm 0.06$ mm.

pattern:

$$\frac{A_p}{m} = \frac{l^2}{N_p} = \lambda^2 \tag{3.1}$$

where $l = 8.0$ cm is the length of the sample side. In Fig. 3.13, A_p is plotted as a function of depth squared, for each type of experiment, with linear fits to the data. A_p is linear with depth squared as expected since λ is linear with depth. We may compare the results of this section with the results of Sec. 3.2. We have, from Eq. 3.1,

$$A_p = m\lambda^2 = k_1 d^2 \tag{3.2}$$

where k_1 is the slope of the line fit to the data. From Sec. 3.2, λ is proportional to depth so we have $\lambda = k_2 d$. We therefore expect that

$$\sqrt{\frac{k_1}{m}} = k_2. \tag{3.3}$$

The results are summarized in Table 2, and show that Eq. 3.3 is satisfied within the experimental uncertainties.

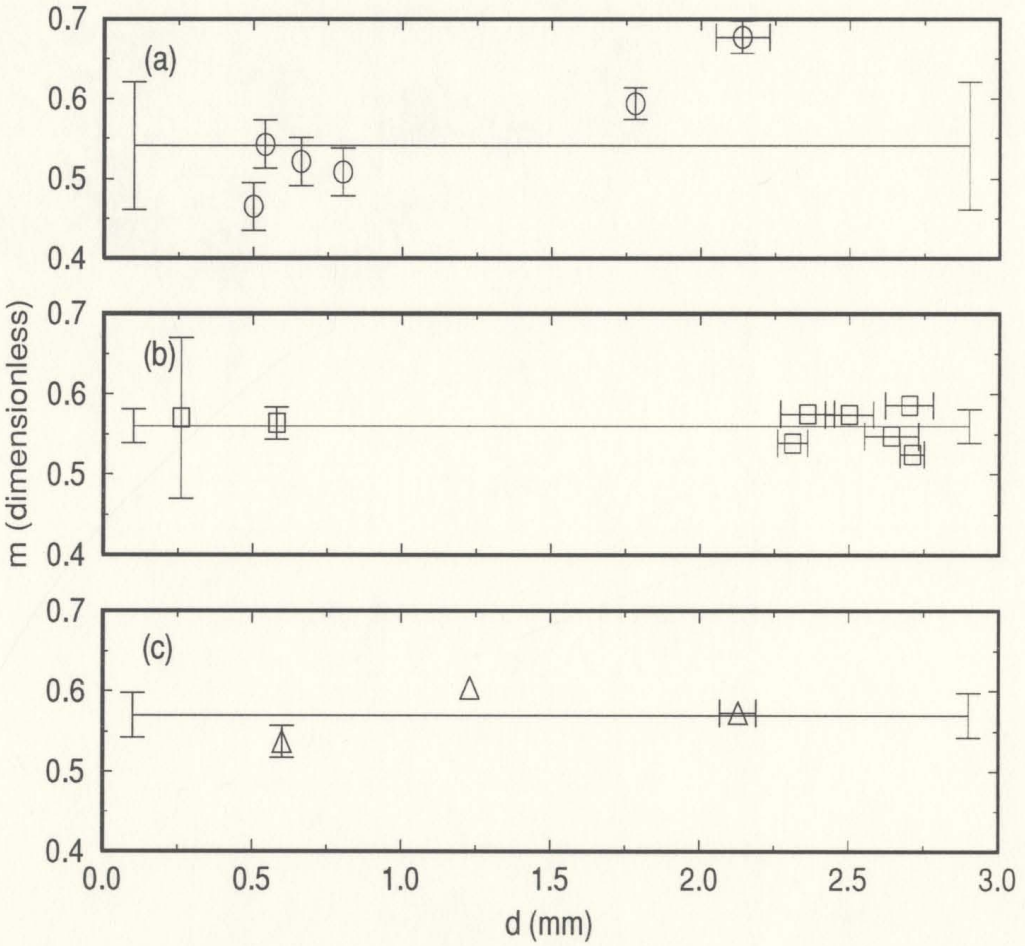

Figure 3.12: The fraction of area which is solid, m as a function of d. The straight line is the mean of the data and the error bars on the lines are the standard deviation of that mean. (a) Type A experiments; $\overline{m}_{\mathrm{A}} = 0.541 \pm 0.080$, (b) Type B experiments; $\overline{m}_{\mathrm{B}} = 0.560 \pm 0.021$, (c) Type C experiments; $\overline{m}_{\mathrm{C}} = 0.570 \pm 0.028$.

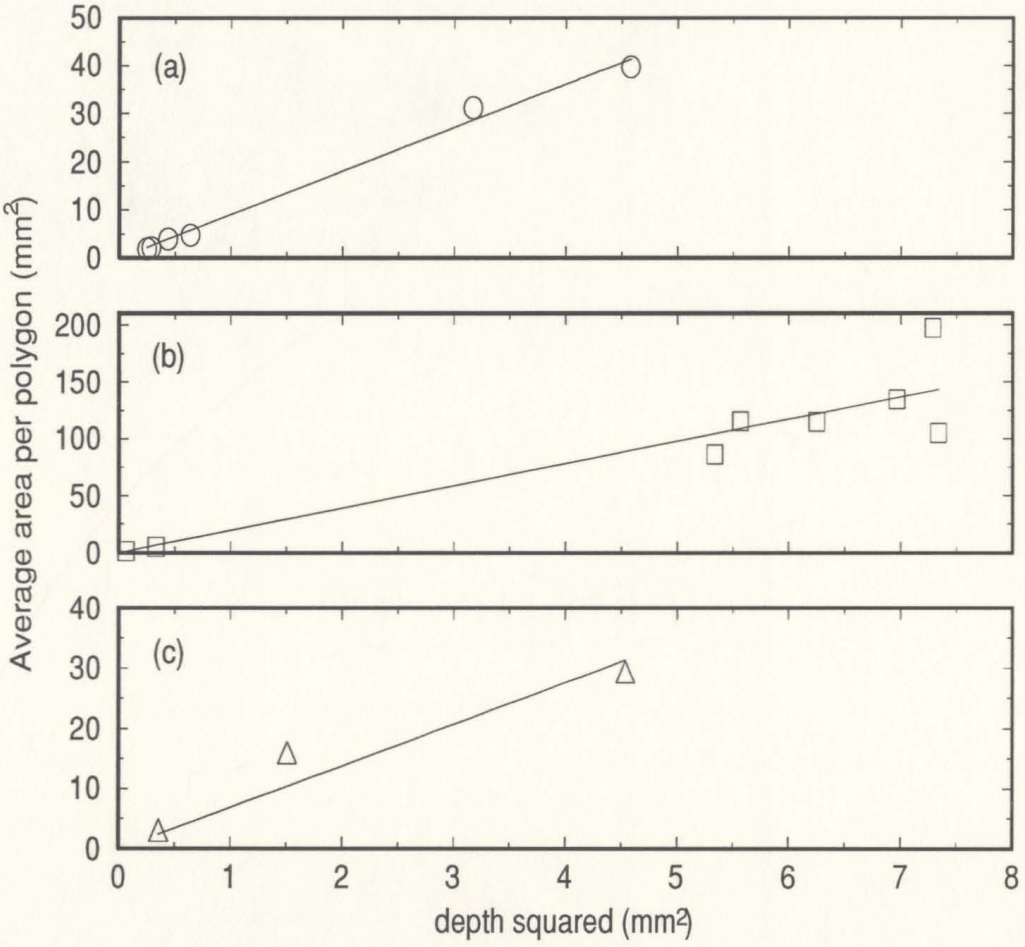

Figure 3.13: A_p as a function of d^2 with linear fits forced through the origin. The error bars are the same size as the symbols. (a) Type A experiments; $A_p = (9.02 \pm 0.26)d^2$, (b) Type B experiments; $A_p = (19.5 \pm 1.7)d^2$, (c) Type C experiments; $A_p = (6.89 \pm 0.88)d^2$.

Type	$\sqrt{k_1/\overline{m}}$	k_2
A	4.08 ± 0.61	3.60 ± 0.08
B	5.90 ± 0.43	6.56 ± 0.26
C	3.48 ± 0.36	3.43 ± 0.04

Table 2: Comparison of the slopes of the linear fits from Figs. 3.2 and 3.13.

3.4 Fourier Transform Analysis

The pattern of cracks has a regularity which lends itself to Fourier analysis. Fourier transform analysis can be used to give information about the spatial structure of a pattern, including its lengthscale. The wavelength of the pattern was calculated in Sec. 3.2 under the approximation that the polygons in the pattern were equal size squares. Fourier analysis reveals the mean lengthscale of the pattern with no prior assumptions about individual fragment size, shape, or orientation. We also analyze the results to extract the correlation length of the pattern and the skewness and kurtosis of the distribution of length scales. The analysis also indicates any preferred orientation of the pattern.

With the mathematical package Matlab, we performed two-dimensional fast Fourier transforms of the images captured with the framegrabber. The Matlab program written for this analysis is given in Appendix A. The Fourier transform of the pattern is complex, and is a function of the wavevector $\vec{k}$. We found the power spectrum of the pattern by multiplying the Fourier

transform by its complex conjugate:

$$P(\vec{k}) = F(\vec{k})F^*(\vec{k}). \tag{3.4}$$

The power spectrum is a real function of $\vec{k}$. We chose the maximum value of k to be 0.5 in units of inverse pixels so that the image was sampled at the Nyquist frequency.

The power spectrum had the form of a central peak with a surrounding ring. The central peak was due to large scale nonuniformities of illumination. Figs. 3.14 – 3.16 are images of typical patterns with their power spectra. The patterns in these figures have a larger area than the patterns in Figs. 3.3 – 3.11. In each of the figures, (a) and (b) are for a thin layer and (c) and (d) are for a thick layer. The rings in the power spectra for the thick layers in the Type A and Type B experiments, Fig. 3.14 (d) and Fig. 3.15 (d), are anisotropic which implies an overall orientation of the pattern in real space as observed in Fig. 3.14 (c) and Fig. 3.15 (c). A layer of similar thickness of Type C experiment, Fig. 3.16 (c) and (d), has a more isotropic power spectrum and the pattern has less directional orientation. The thinner layers of all experiments have approximately isotropic power spectra.

The central peak was removed and the azimuthal average of the power spectrum was taken to obtain a smoother profile and eliminate anisotropic effects. Figs. 3.17 – 3.19 show $kP(k)$, where $P(k)$ is the averaged power spectra as a function of wavenumber k for the runs in Figs. 3.14 – 3.16. The data are peaked about some wavenumber k_c which was determined by fitting a parabola to the peak of the distribution. The fit of the the average power

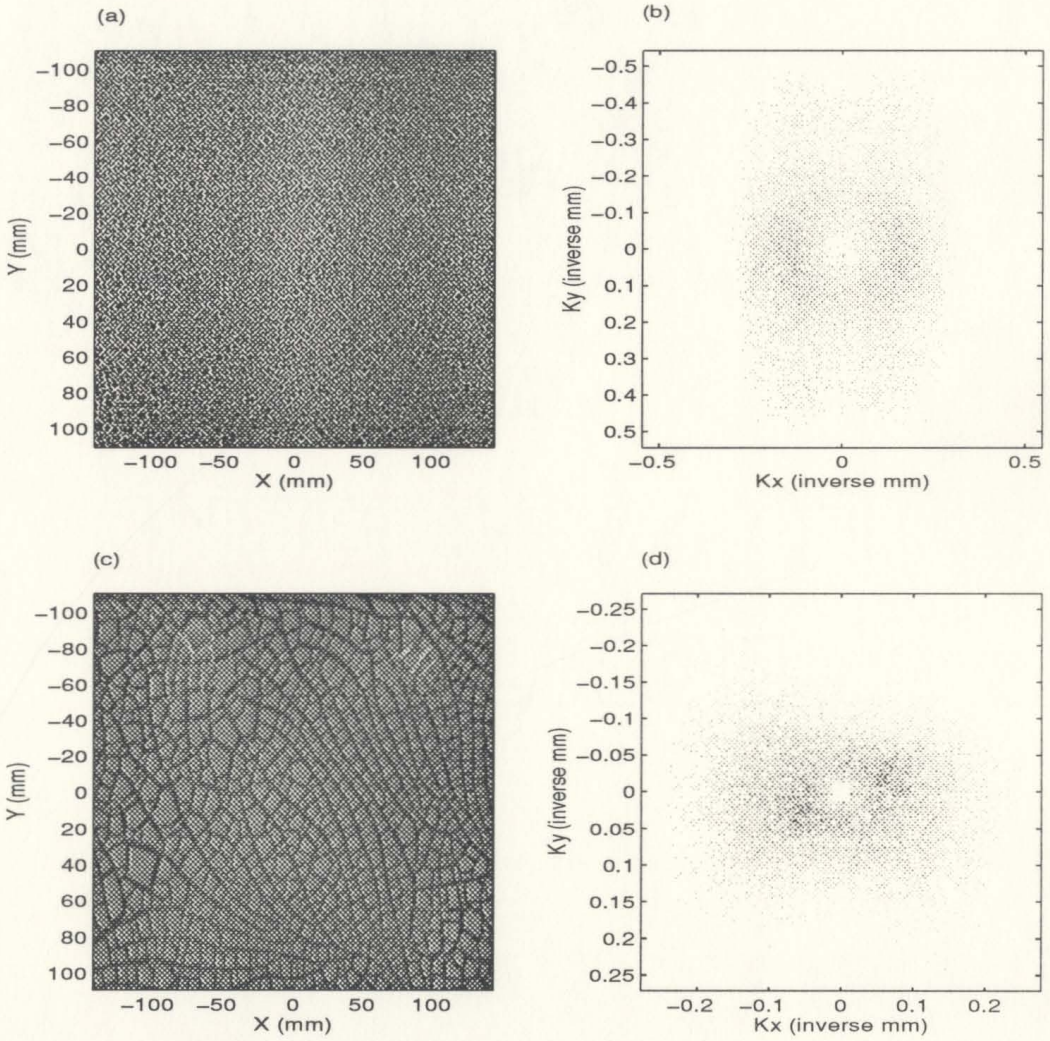

Figure 3.14: Images and power spectra of Type A experiments. (a) Image of sample area with $d = 0.49 \pm 0.07$ mm, (b) power spectrum of (a), (c) image of sample area with $d = 1.93 \pm 0.21$ mm, (d) power spectrum of (c).

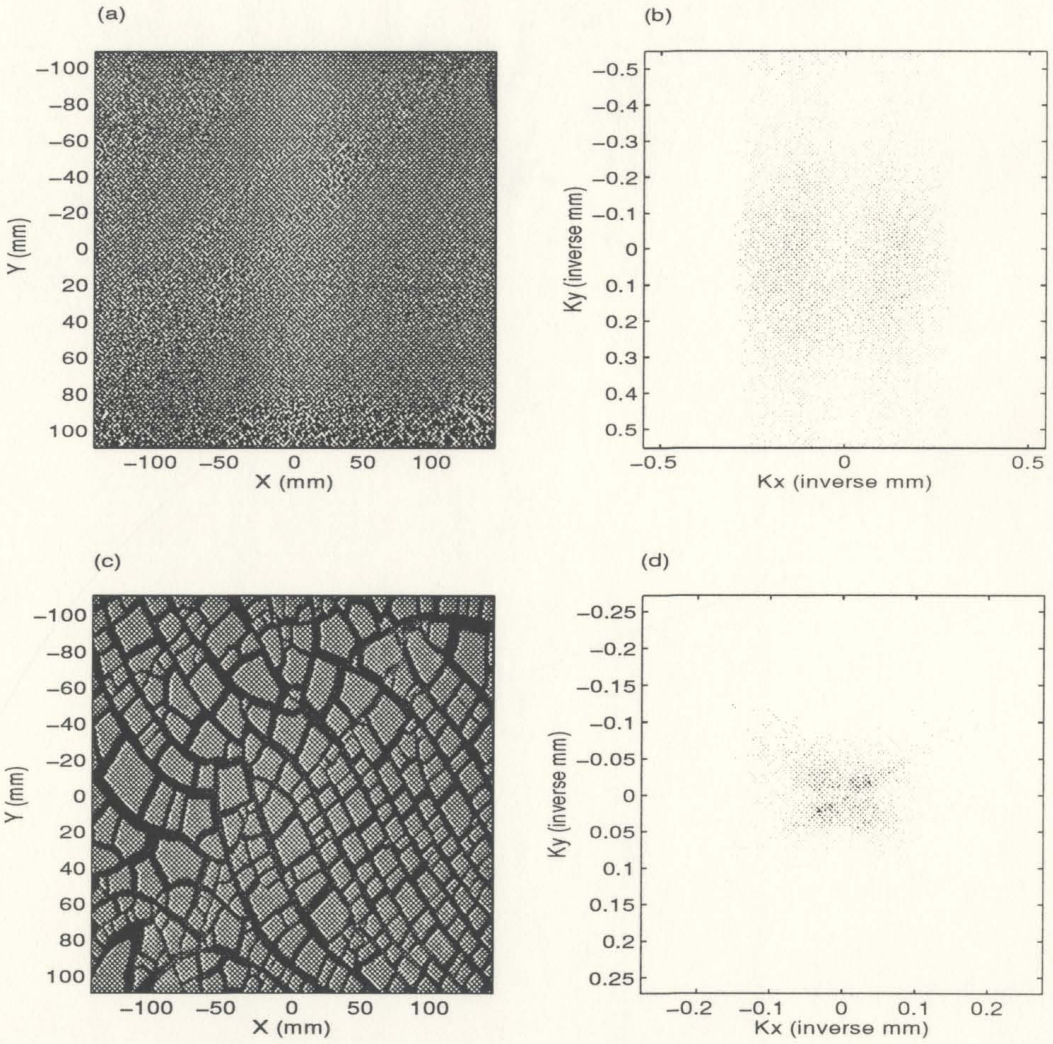

Figure 3.15: Images and power spectra with Type B experiments. (a) Image of sample area of $d = 0.28 \pm 0.06$ mm, (b) power spectrum of (a), (c) image of sample area with $d = 2.53 \pm 0.22$ mm, (d) power spectrum of (c).

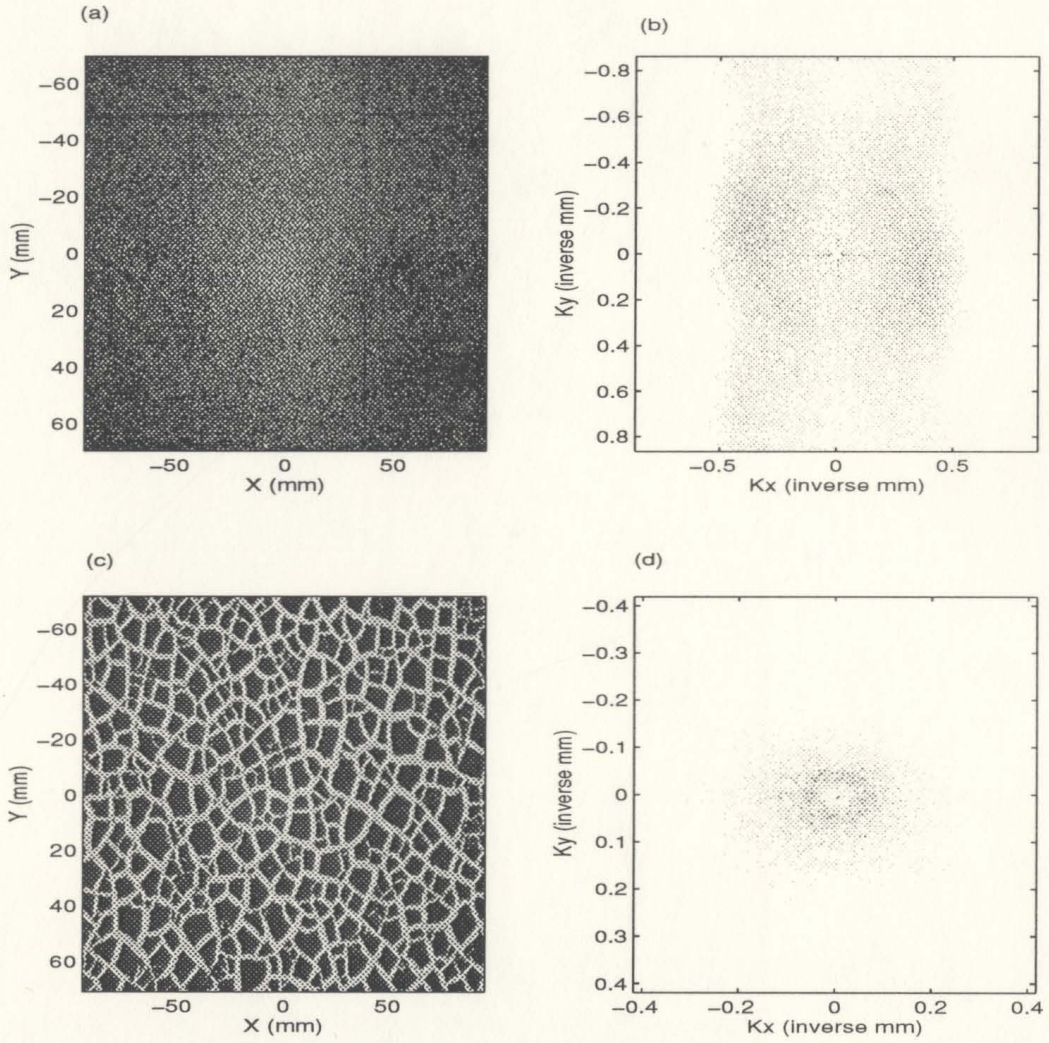

Figure 3.16: Images and power spectra of Type C experiments. (a) Image of sample area with $d = 0.23 \pm 0.02$ mm, (b) power spectrum of (a), (c) image of sample area with $d = 2.13 \pm 0.06$ mm, (d) power spectrum of (c).

spectrum shown in Fig. 3.14(b) is shown in Fig. 3.20. The error in k_c was taken as the greatest amount by which the maximum of the parabola could be shifted and still be a reasonable fit to the data.

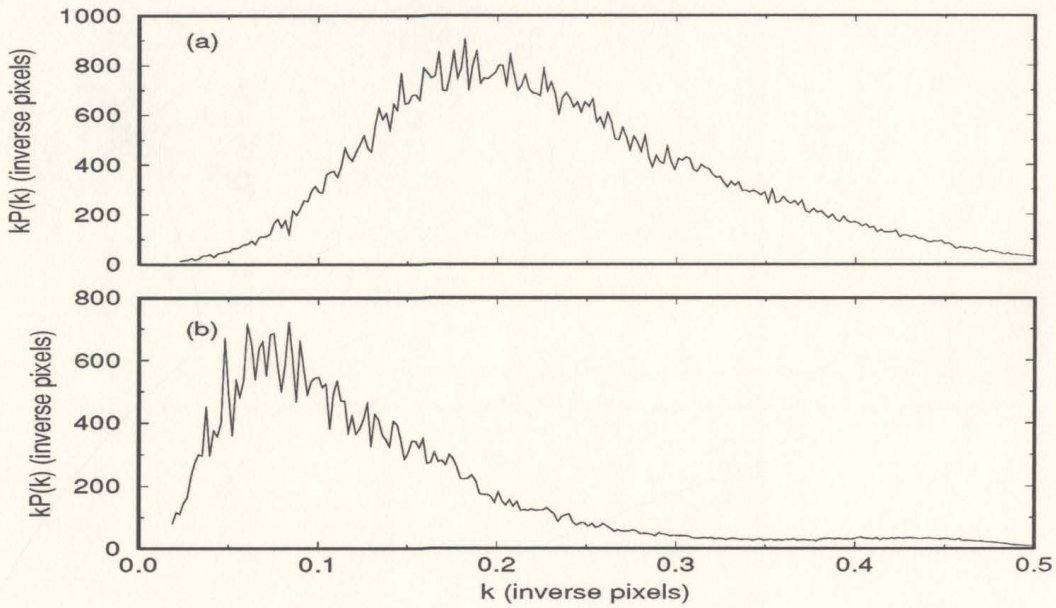

Figure 3.17: Azimuthally averaged power spectra of Type A experiments, (a) $d = 0.49 \pm 0.07$mm, (b) $= 1.93 \pm 0.21$mm.

The lengthscale or wavelength of the pattern is the inverse of k_c, $\lambda = 1/k_c$. The wavelength for each type of experiment is plotted as a function of depth in Fig. 3.21. The wavelength is linear with depth with slopes that agree reasonably well with Sec. 3.2. Fig. 3.22 is a plot of the wavelengths found by Fourier analysis along with the values of λ as found in Sec. 3.2. The two methods of finding the lengthscale of the pattern are consistent.

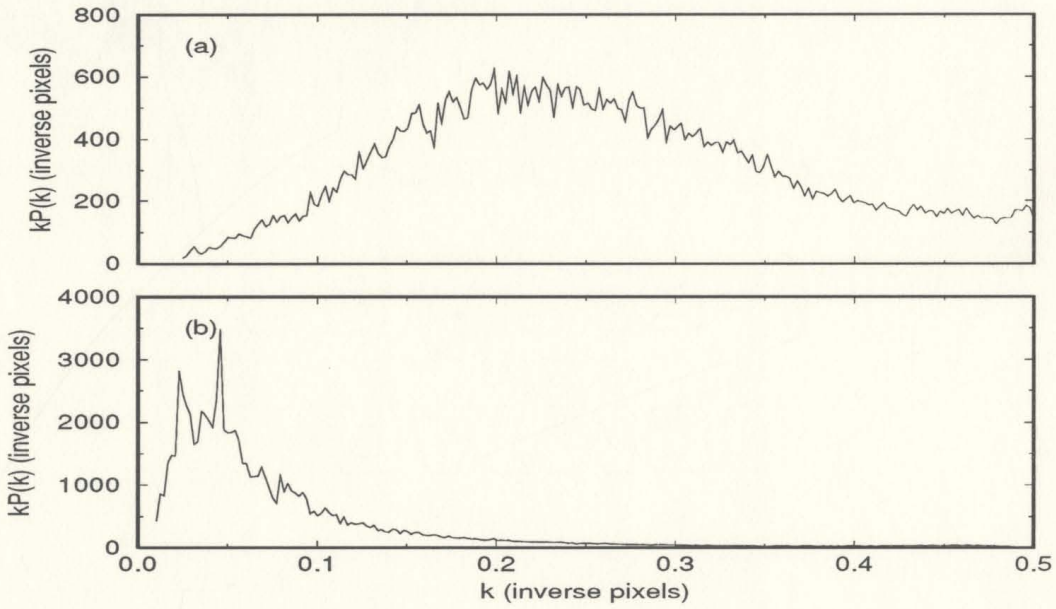

Figure 3.18: Azimuthally averaged power spectra of Type B experiments, (a) $d = 0.28 \pm 0.06$mm, (b) $d = 2.53 \pm 0.22$mm.

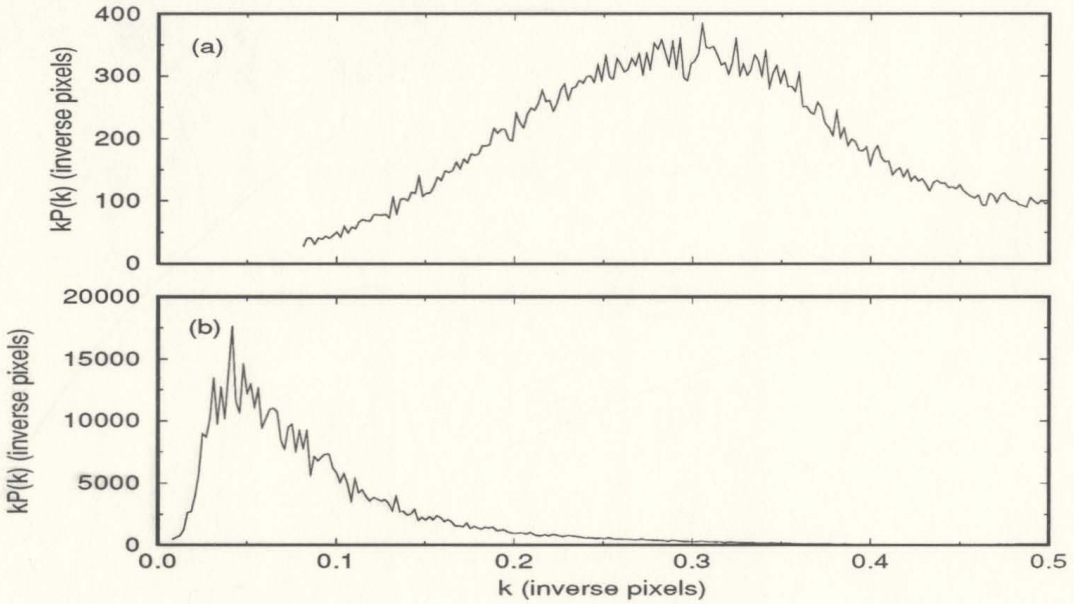

Figure 3.19: Azimuthally averaged power spectra of Type C experiments, (a) $d = 0.23 \pm 0.02$mm, (b) $d = 2.13 \pm 0.06$mm.

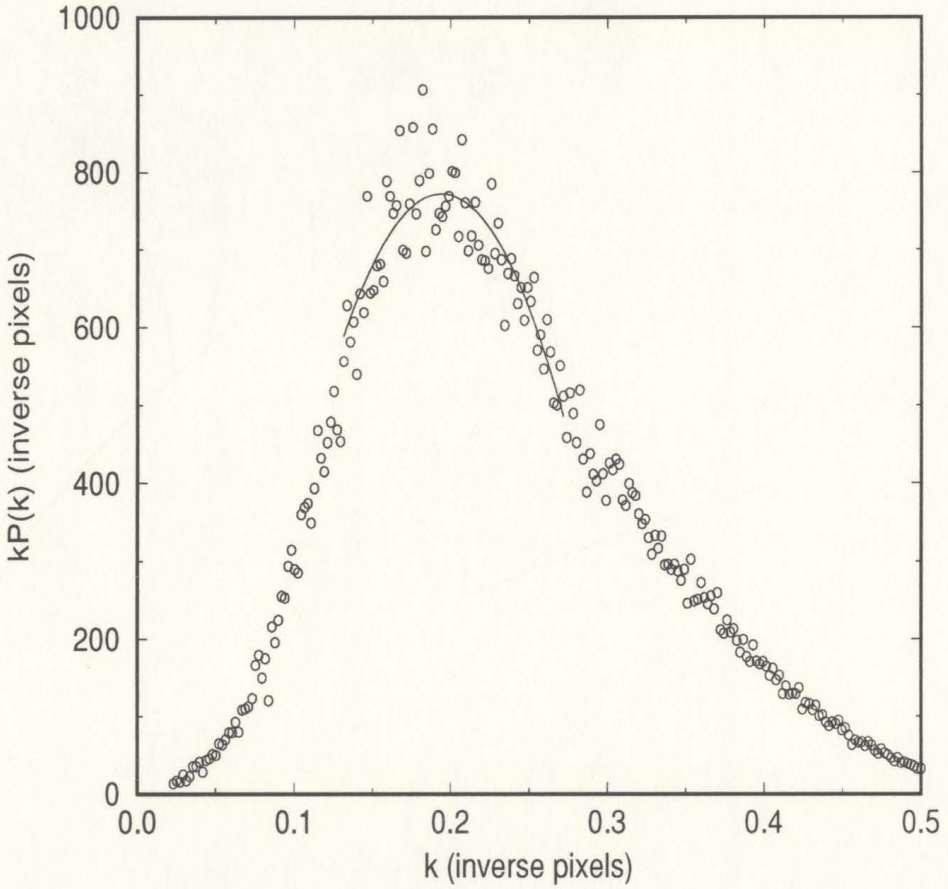

Figure 3.20: Parabola fit to the tip of $kP(k)$ distribution of Type A experiment with $d = 0.49 \pm 0.07$ mm.

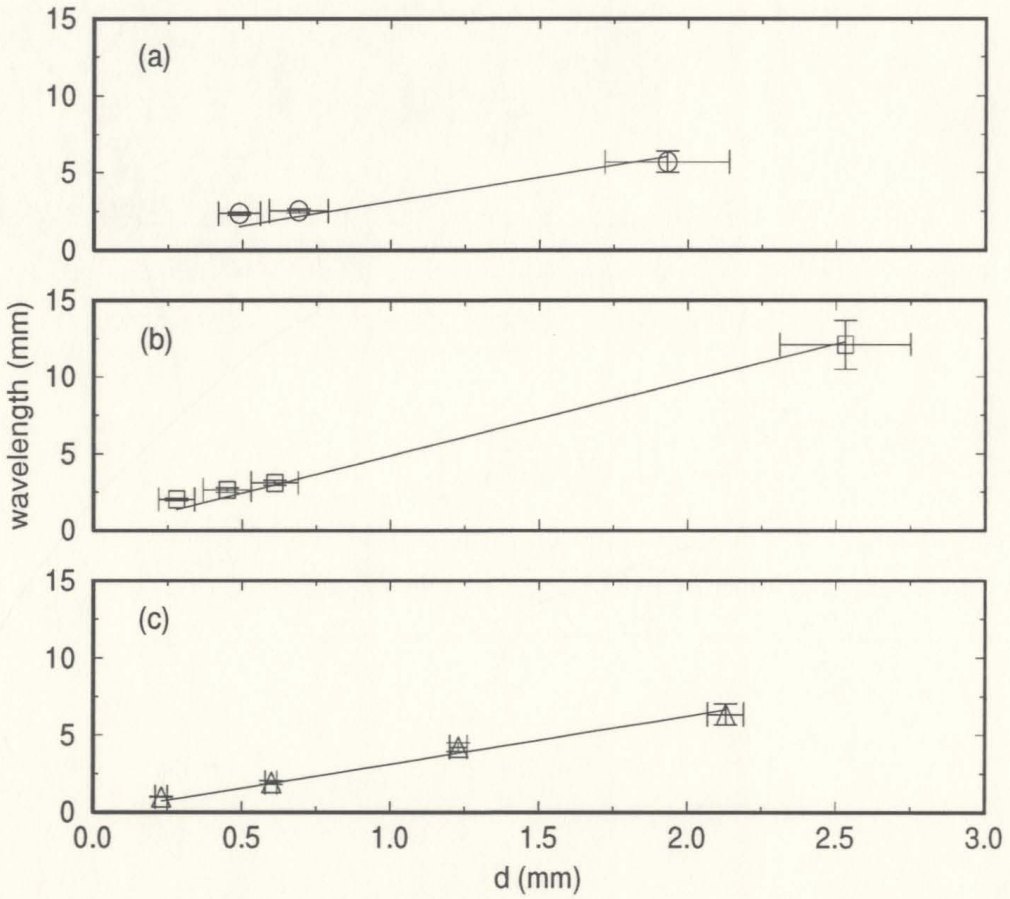

Figure 3.21: The wavelength of the pattern ($\lambda = 1/k_c$) as a function of d with linear fits forced through the origin. (a) Type A experiments; $\lambda = (3.14 \pm 0.33)d$, (b) Type B experiments; $\lambda = (4.86 \pm 0.18)d$, (c) Type C experiments; $\lambda = (3.11 \pm 0.13)d$.

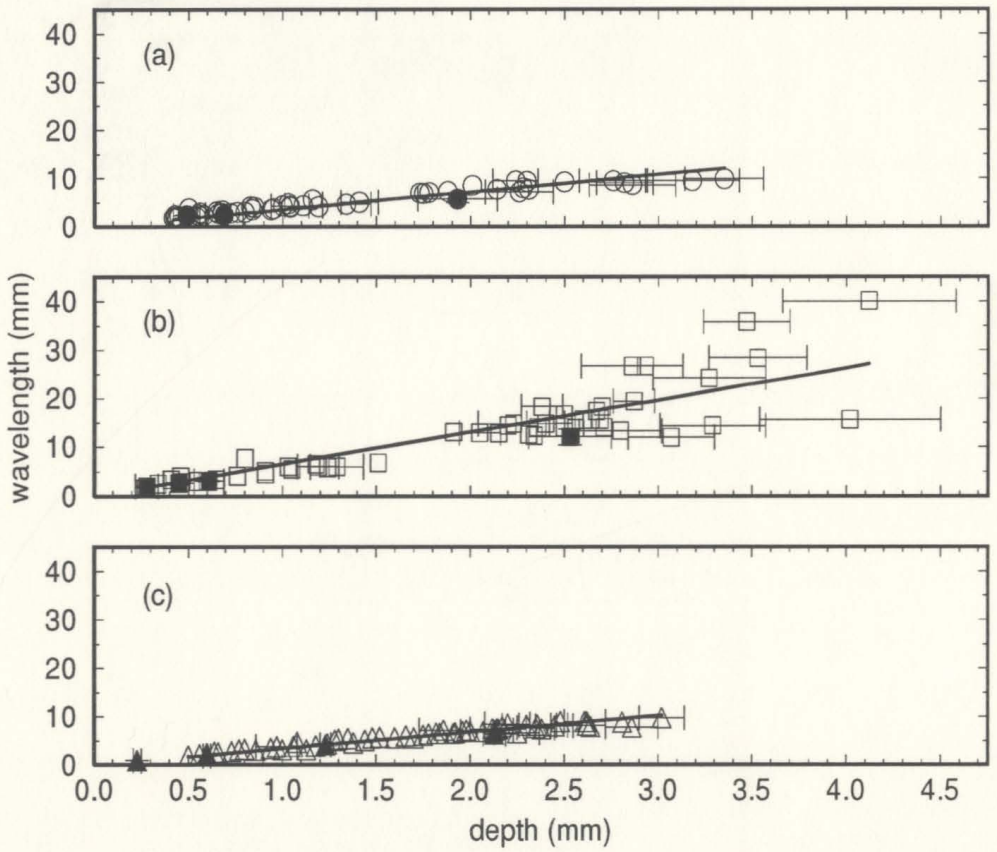

Figure 3.22: The wavelength of the pattern from the Fourier analysis (solid symbols) and the wavelength as found in Sec. 3.2 (open symbols) as a function of d, (a) Type A experiments, (b) Type B experiments, (c) Type C experiments.

The mean spatial frequency of the data is defined by

$$\langle k \rangle \equiv \frac{\int |\vec{k}| P(\vec{k}) d^2\vec{k}}{\int P(\vec{k}) d^2\vec{k}} = \frac{\int_0^\infty k^2 P(k) dk}{\int_0^\infty k P(k) dk}. \tag{3.5}$$

The moments μ_n of $P(k)$ about $\langle k \rangle$ are defined by

$$\mu_n = \left[\frac{\int (|\vec{k}| - \langle k \rangle)^n P(\vec{k}) d^2\vec{k}}{\int P(\vec{k}) d^2\vec{k}} \right] = \left[\frac{\int_0^\infty (k - \langle k \rangle)^n k P(k) dk}{\int_0^\infty k P(k) dk} \right]. \tag{3.6}$$

The μ_n were calculated numerically by quadrature with Matlab. Quadrature is a method by which the data are fitted to a polynomial and a remainder term. The integral is approximated by summing the fitting function over the range of data.

The standard deviation σ was calculated from the second moment with $\sigma = \sqrt{\mu_2}$. The standard deviation as a function of depth is plotted in Fig. 3.23. The error in σ is taken to be the scatter in the data. The correlation length ξ which characterizes the range over which the pattern is ordered is given by $\xi = 1/\sigma$. In Fig. 3.23 we see that standard deviation is constant with depth which implies that the range of order is constant with depth. Except in thin layers, $\xi \leq \lambda$, which means that while for thin layers, the pattern is correlated over several wavelengths, for thick layers the correlation length is smaller than a wavelength. The average correlation length, $\bar{\xi} = 1/\bar{\sigma}$, changes with the type of experiment. For Type A, $\bar{\xi_A} = 5.1 \pm 0.1$ mm, for Type B, $\bar{\xi_B} = 4.8 \pm 0.5$ mm, and for Type C, $\bar{\xi_C} = 3.4 \pm 0.4$ mm. The average spacing between the impurities in Type C experiments is about 4 mm. This suggests that the shorter range of order in the Type C experiments, is due to the impurities. The smaller correlation length for Type C indicates that

experiments with added impurities had a lower range of order, consistent with expectations.

The skewness $\mathcal{S}$ was calculated from the second and third moments as $\mathcal{S} = \mu_3 \mu_2^{-\frac{3}{2}}$. Skewness is a measure of the deviation from symmetry about the mean of the distribution and is dimensionless. The error in skewness was taken to be the difference in skewness between an outer and inner envelope drawn around the data. Positive skewness means that the distribution is asymmetric with a tail extending out toward more positive k. A skewness of zero indicates a symmetrical distribution and a negative value signifies an asymmetric distribution with the tail extending out toward more negative k. In all experiments the skewness is positive and increases approximately linearly as a function of depth as shown in Fig. 3.24. It is close to zero only for the thinnest Type C layer ($d = 0.23 \pm 0.02$ mm).

The excess kurtosis κ was calculated from the fourth and second moments as $\kappa = \mu_4 \mu_2^{-2} - 3$, where the excess kurtosis has been defined to be zero for a gaussian. Kurtosis is the degree of peaking relative to a gaussian and is dimensionless. A sharp peak has positive excess kurtosis and a flatter peak has a negative value. The excess kurtosis is plotted as a function of depth in Fig. 3.25. For all three sets of experiments, the excess kurtosis is close to zero for thin layers and increases approximately linearly with depth.

These results imply that for the thinnest layers the Fourier power spectrum is close to gaussian, but becomes more asymmetrical and more sharply peaked with depth. The skewness and excess kurtosis do not have a direct,

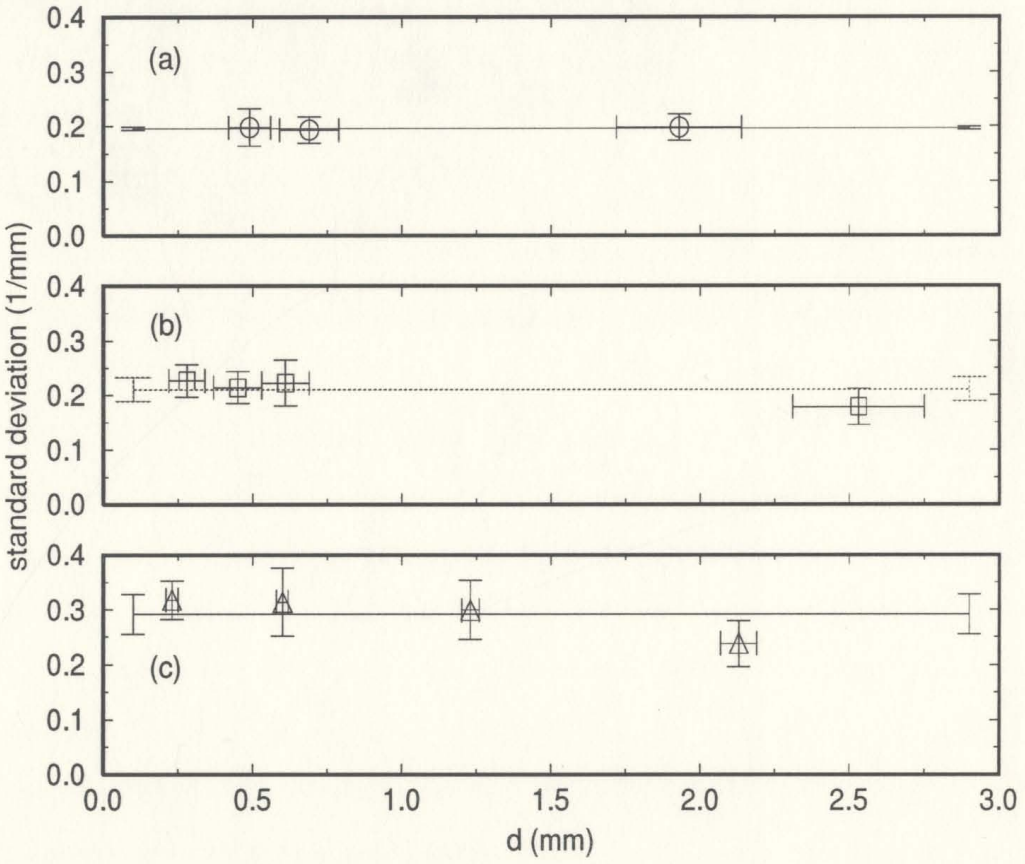

Figure 3.23: The standard deviation σ as a function of d. The lines are the mean value, $\bar{\sigma}$ and the error bars on the lines are the standard deviation. (a) Type A experiments; $\bar{\sigma} = 0.197 \pm 0.003$ mm^{-1}, (b) Type B experiments; $\bar{\sigma} = 0.210 \pm 0.022$ mm^{-1}, (c) Type C experiments; $\bar{\sigma} = 0.292 \pm 0.037$ mm^{-1}.

simple relationship to the pattern in real space, but these values may be useful in classifying the patterns or for comparisons between experimental and numerical results.

The data were also fit to a gaussian form,

$$kP(k) = \frac{N}{\sqrt{2\pi}\,\sigma} \exp\left(-\frac{(k-k_c)}{2\sigma^2}\right) \tag{3.7}$$

where N is a fitting parameter, σ is the standard deviation calculated numerically, and k_c is the mode, determined by fitting a parabola to the peak of the $kP(k)$ distribution. The fit is adequate only for the thinnest layer of Type C ($d = 0.23 \pm 0.02$ mm) as seen in Fig. 3.26. Even for this experiment, the fit fails for $k > 0.4$ inverse pixels. There is a high-k tail in the distribution which is also indicated by the nonzero skewness from Fig. 3.24.

In the Type C experiment of depth 0.23 ± 0.02 mm, which has the $kP(k)$ distribution closest to a gaussian, the location of the cracks is probably primarily determined by the location of the impurities which is approximately random. In the other runs, the nongaussian power spectrum that the location of cracks is not random, but has some distribution which depends on the stress field surrounding the crack.

3.5 Number of Sides Per Polygon as a Function of Depth

For depths of from 0.5 mm to several millimetres we counted the number of sides per polygon for each different type of experiment. Fig. 3.27 is a histogram showing the number of polygons with n sides as a function of n

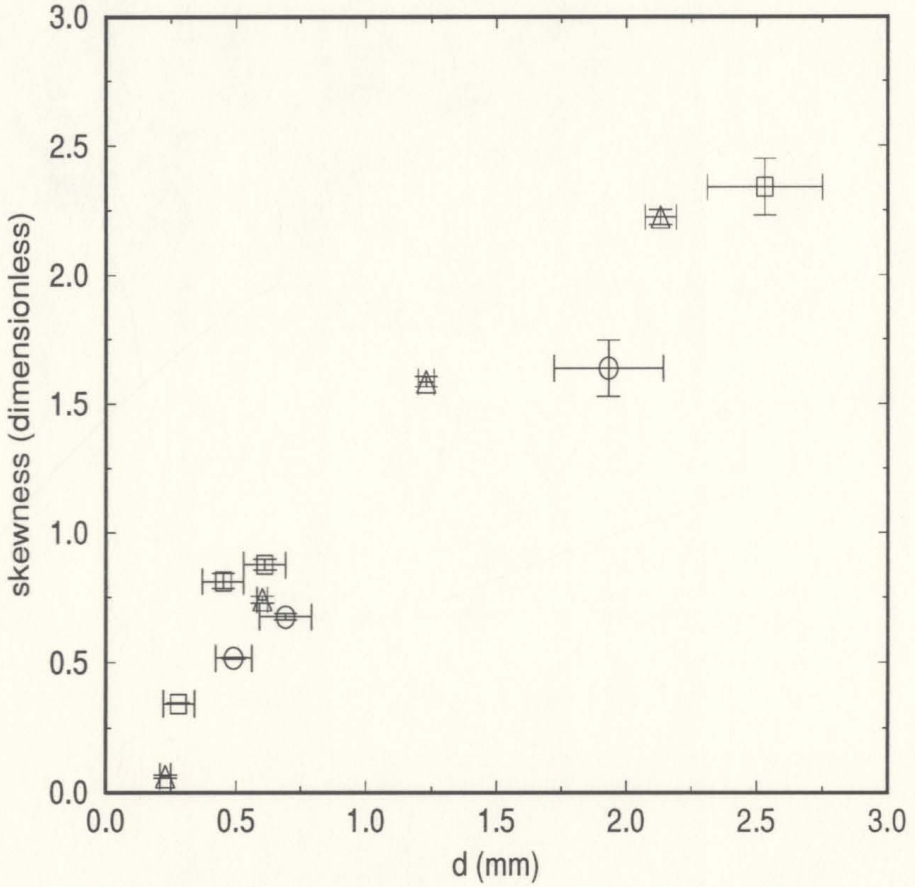

Figure 3.24: The skewness, $\mathcal{S}$ as a function of d for Type A experiments (circles), Type B experiments (squares), and Type C experiments (triangles).

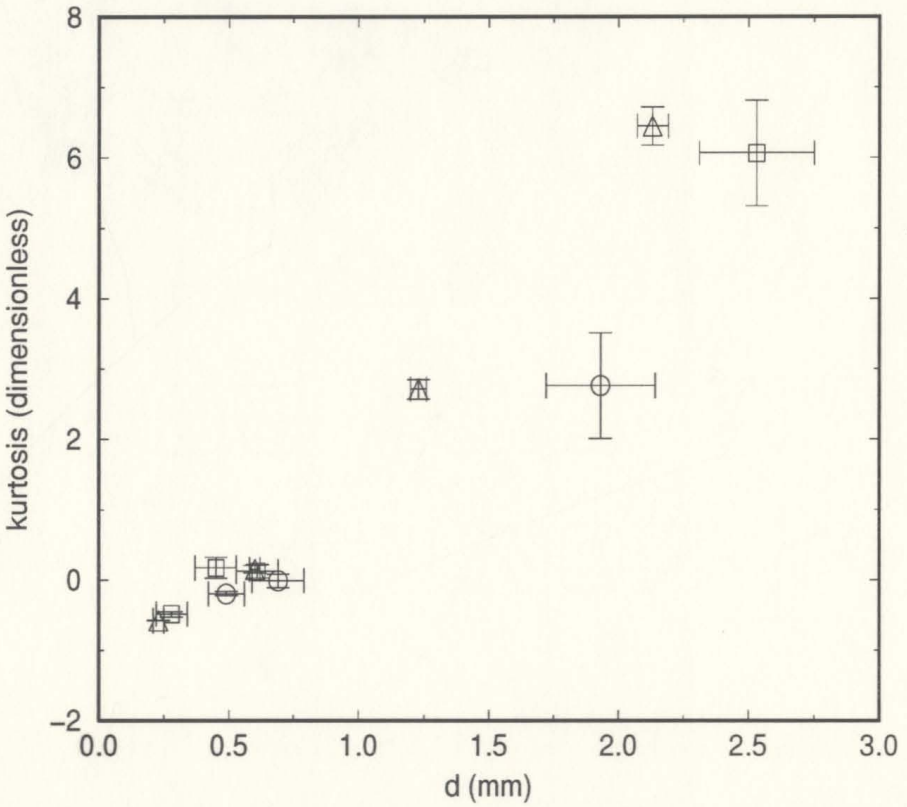

Figure 3.25: The kurtosis, κ as a function of d for Type A experiments (circles), Type B experiments (squares), and Type C experiments (triangles).

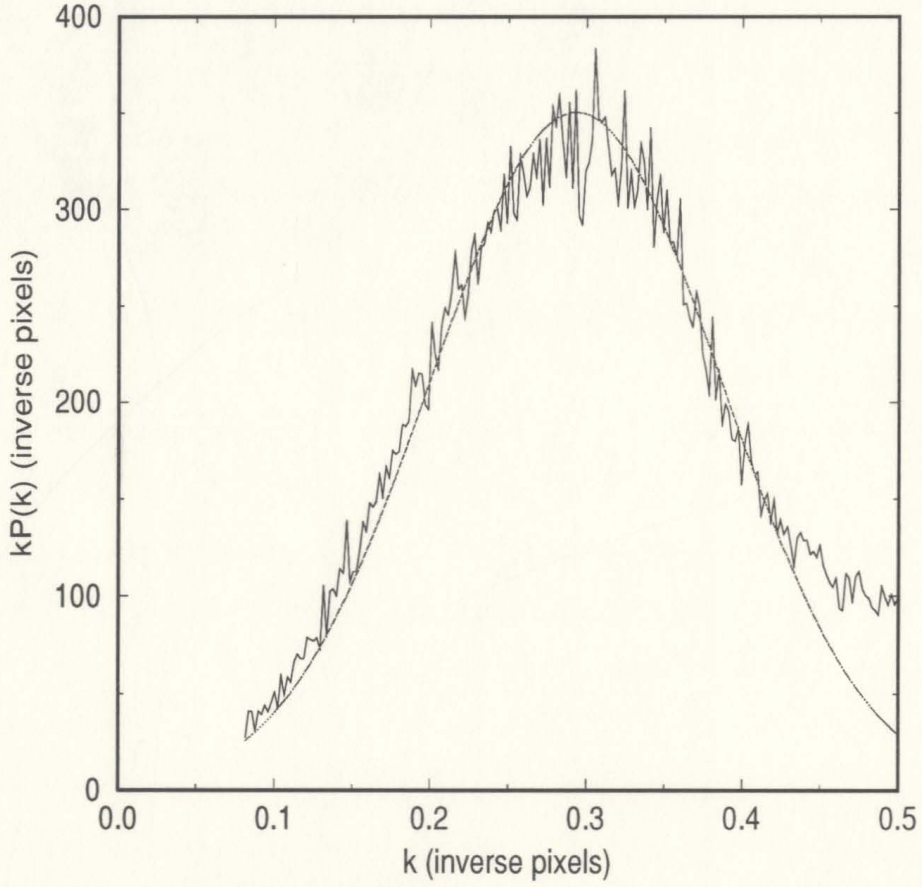

Figure 3.26: $kP(k)$ as a function of k for a Type C experiment with $d = 0.23 \pm 0.02$ mm with a gaussian fit.
$kP(k) = (81.4 \pm 0.6)/\sqrt{2\pi}\ \sigma \exp\left[-(k - k_c)^2/2\sigma^2\right]$

for a typical run of each type of experiment. In each subplot the depth of the layers are approximately equal. The histogram shows that there were similar numbers of polygons with n sides for Type A and Type C experiments and consistently fewer for the Type B experiments with the same depths since the Type B polygons were larger. In all cases, the distributions of polygons are similar. The plot indicates that the polygons were primarily four sided with approximately equal numbers of three and five sided polygons and few six sided polygons.

Figs. 3.28 and 3.29 show the unbinned data of percentage of three and four sided polygons as a function of depth for each type of experiment. To reduce the scatter, the data were then divided into bins 0.5 mm wide and the average value of N_p for each depth bin was calculated. On average, there are 5 points in each bin. Figs. 3.30 – 3.33 show the binned data as histograms showing the percentage of polygons with n sides, where n ranges from 3 to 6, as a function of d. The error bars are the standard deviation of the points in the bin.

The data in Figs. 3.28 and 3.29(a) and (b) indicate a transition at a depth of 1.5 mm in Types A and B experiments. For layers thicker than this depth, there is a greater amount of scatter in the data, and the percentage of 3 sided polygons is decreased while the percentage of 4 sided polygons is increased. The percentages do not change in the Type C runs. At greater depths, there is a wider scatter about the mean lengthscale, as can be seen in Figs. 3.2(a) and (b), which show a scatter in the number of polygons in the sample area

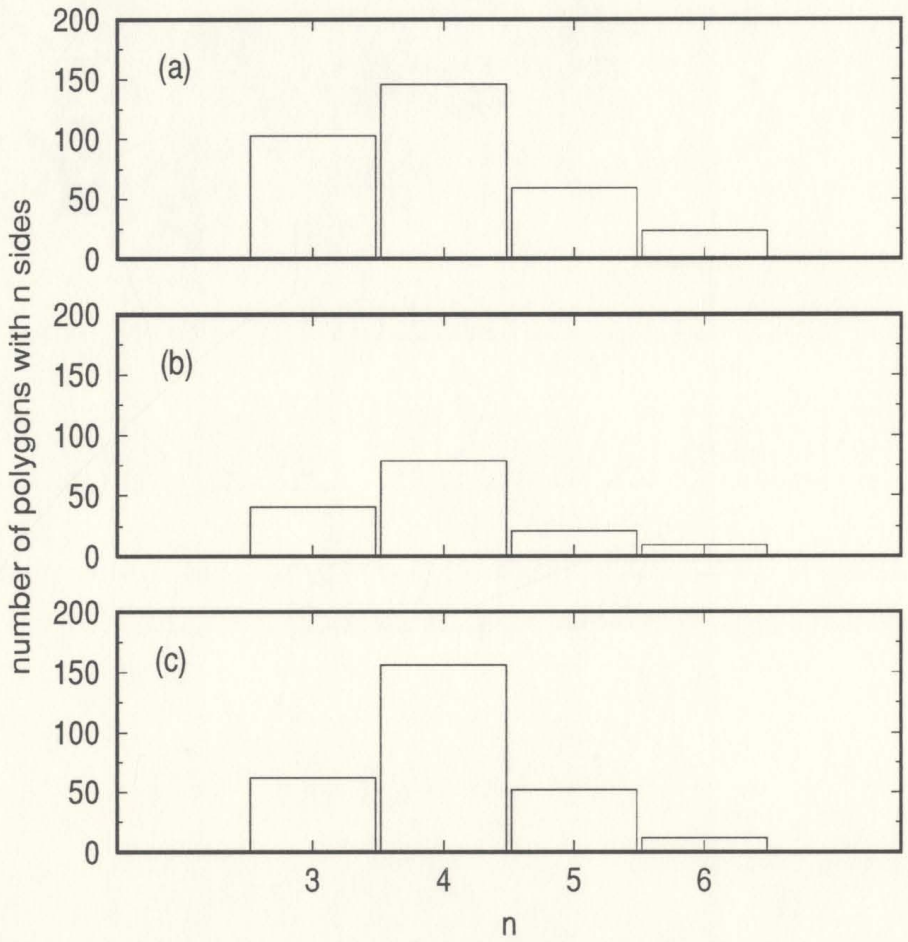

Figure 3.27: Number of sides n per polygon as a function of n. (a) Type A experiment, $d = 1.11 \pm 0.10$ mm, (b) Type B experiment, $d = 1.18 \pm 0.09$ mm, (c) Type C experiment, $d = 1.08 \pm 0.05$ mm.

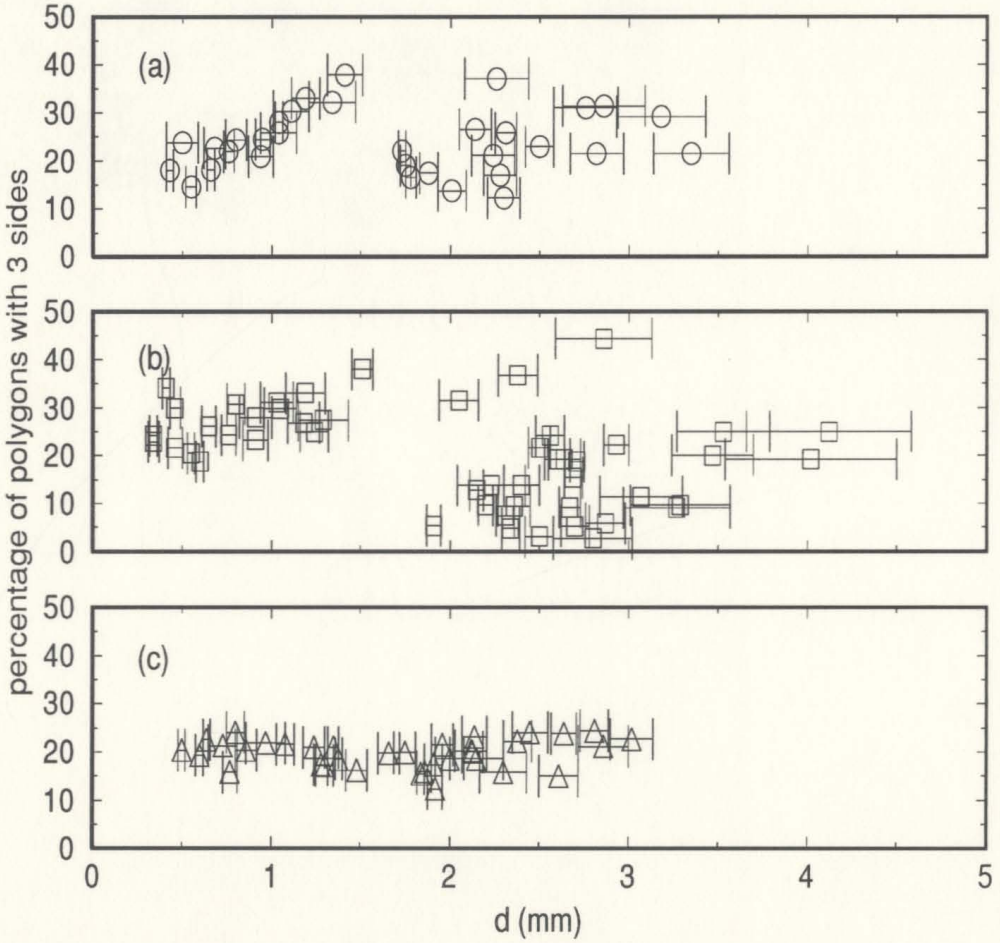

Figure 3.28: Percentage of three sided polygons as a function of d. (a) Type A experiments, (b) Type B experiments, and (c) Type C experiments.

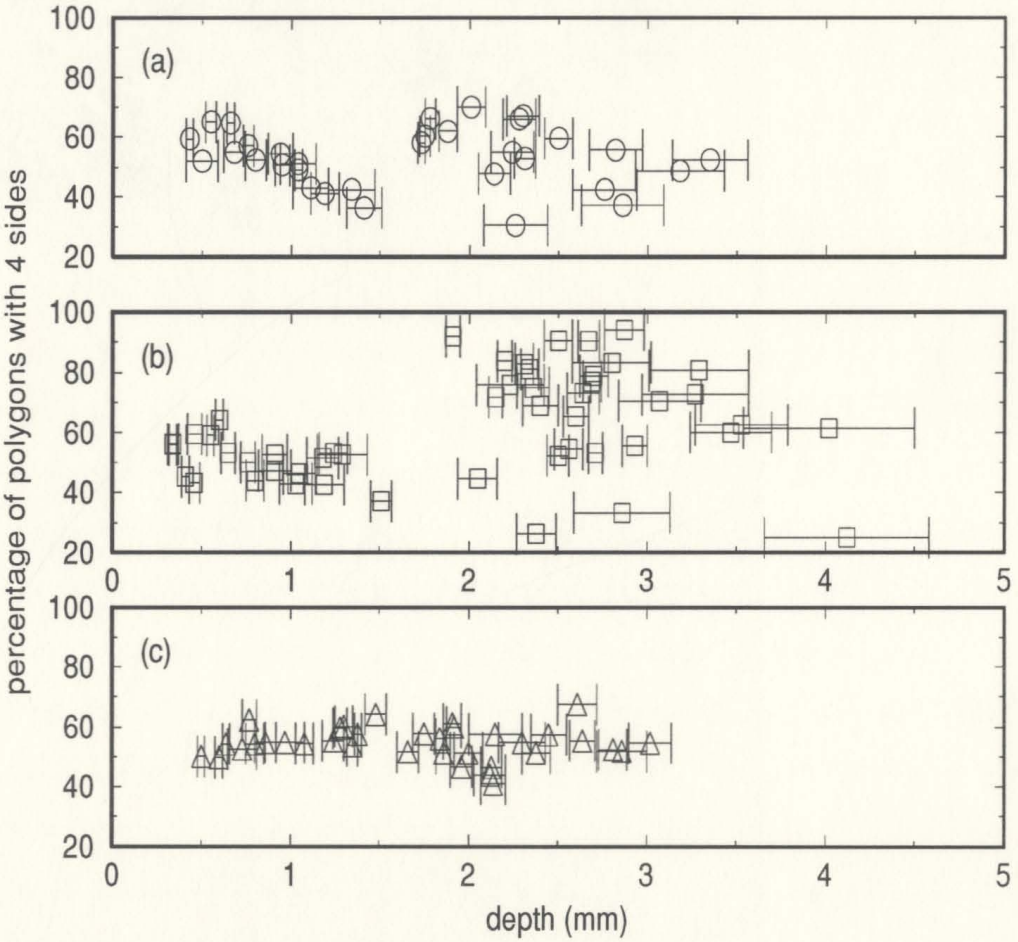

Figure 3.29: Percentage of four sided polygons as a function of d. (a) Type A experiments, (b) Type B experiments, and (c) Type C experiments.

for Types A and B experiments. For thicker depths the sample areas have fewer polygons and statistical fluctuations may lead to more scatter in the data. Despite this the histograms in Figs. 3.30 and 3.31 (a) and (b) do seem to indicate a transition at a depth of about 1.5 mm to more 4 sided polygons and fewer 3 sided polygons. The histogram in Fig. 3.32(b) shows that there may be a transition to a decreased number of 5 sided polygons in Type B experiments at depths greater than 1.5 mm. The number of 6 sided polygons stays approximately constant, within the scatter, with depth for all experiments as seen in Fig. 3.33.

The late stages of individual polygon formation may change with depth. In the thinner layers of Type A and Type B experiments, as the initial pattern of polygons is in the final stages of drying, the individual polygons contract further and the adhesion to the substrate causes another fracture. These fractures tend to form along corners of the polygons, as shown in Fig. 3.34, creating pairs of 3 and 4 sided polygons or 3 and 5 sided polygons. This fragmentation is not as common in the thicker layers. Figs. 3.1 and 3.35 are images of a thin and thick layer of Type A. Figs. 3.36 and 3.37 are images of a thin and thick layer of Type B. These images are approximately 16 cm by 16 cm in real space. The thin layers in Type A and Type B runs seem to have more fragmented polygons.

There is no noticeable transition seen in the percentages of Type C experiments, and the thin layer of a Type C pattern, shown in Fig. 3.38, does not seem to have many fragmented polygons. In Type C experiments, the

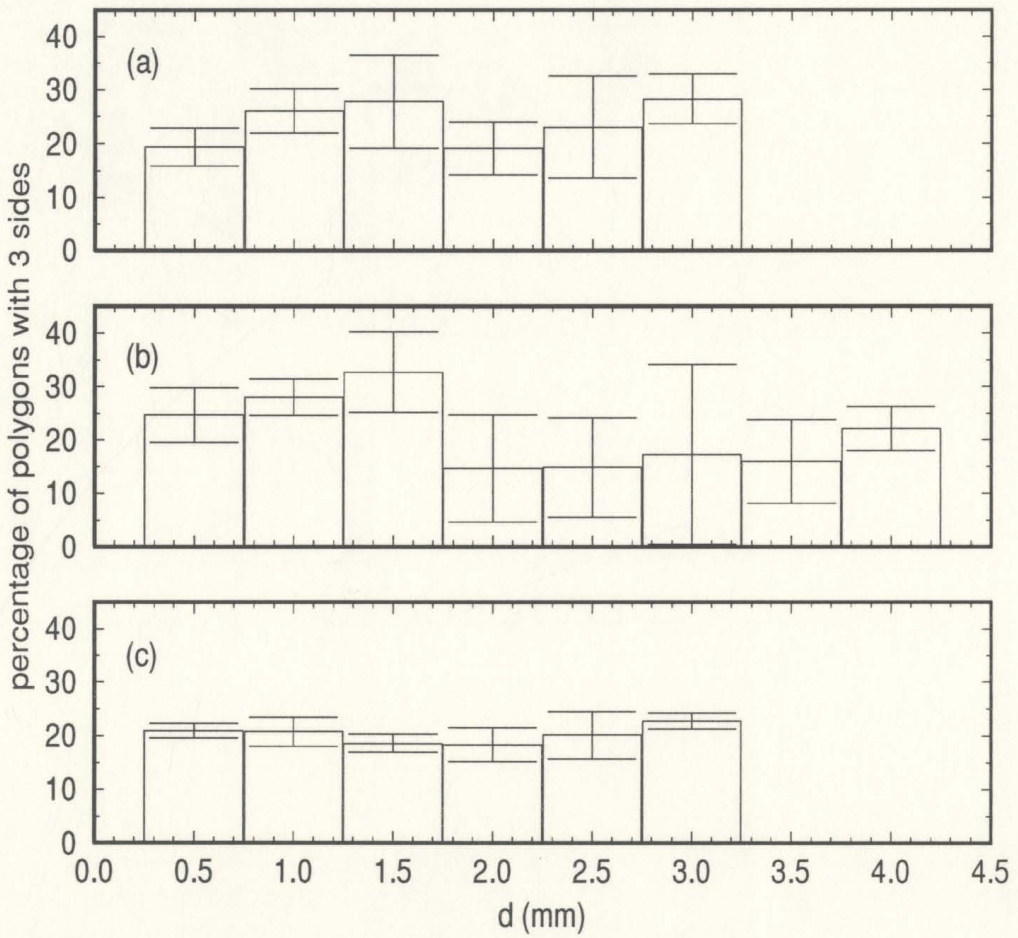

Figure 3.30: Percentage of three sided polygons as a function of d. The straight line is the mean over depth of the percentages. (a) Type A experiments, (b) Type B experiments, (c) Type C experiments.

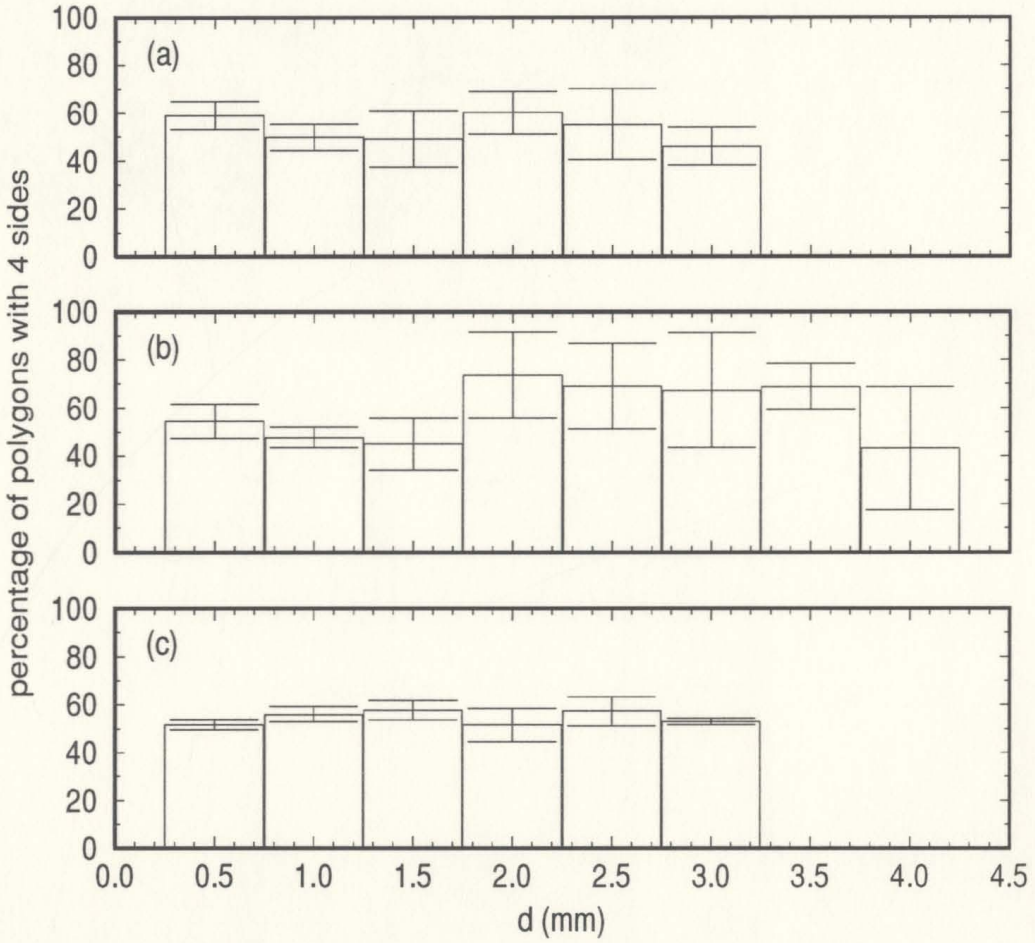

Figure 3.31: Percentage of four sided polygons as a function of d. (a) Type A experiments, (b) Type B experiments, (c) Type C experiments.

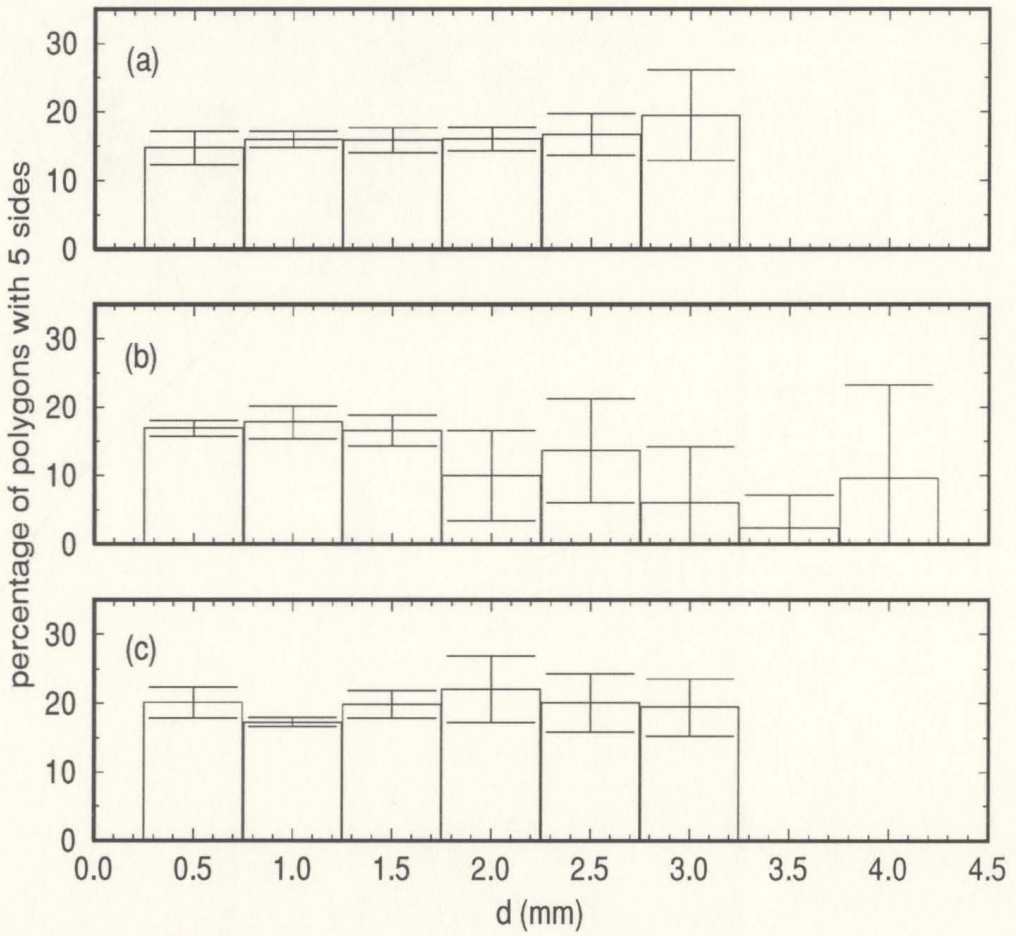

Figure 3.32: Percentage of five sided polygons as a function of d. (a) Type A experiments, (b) Type B experiments, (c) Type C experiments.

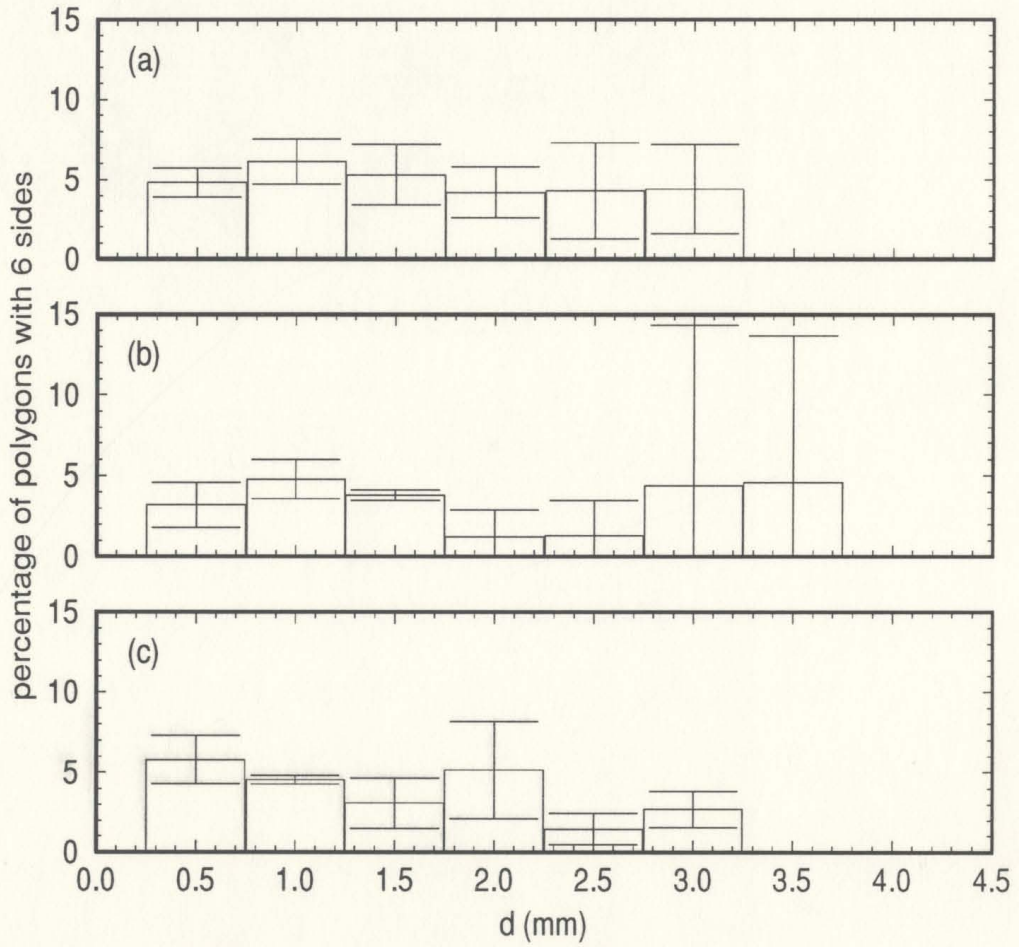

Figure 3.33: Percentage of six sided polygons as a function of d. (a) Type A experiments, (b) Type B experiments, (c) Type C experiments.

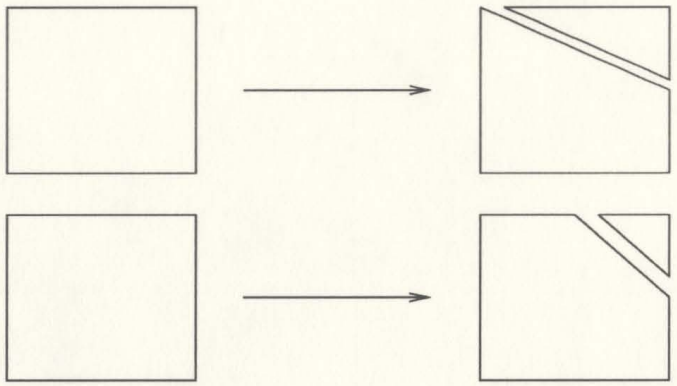

Figure 3.34: Illustration of how polygons split

later stage polygon fragmentation probably does not occur because the fractures, which have locations determined by the impurities, are spaced closely enough that the polygons do not shrink sufficiently to increase the stress to a breaking value.

In all experiments, most of the 4 sided polygons form with straight edges and have 90° angles at the corners. Since all patterns have mostly 4 sided polygons, we expect that most junction angles will be perpendicular. Many of the polygons with other numbers of sides, particularly the 3 sided polygons, have curved edges and while some of the intersections are non perpendicular, many cracks meet at 90° as can be seen, for example, in Fig. 3.37. Decreased numbers of 4 sided polygons lead us to expect that the scatter of junction angles may be wider but these data cannot give quantitative information about the distribution of junction angles in the pattern.

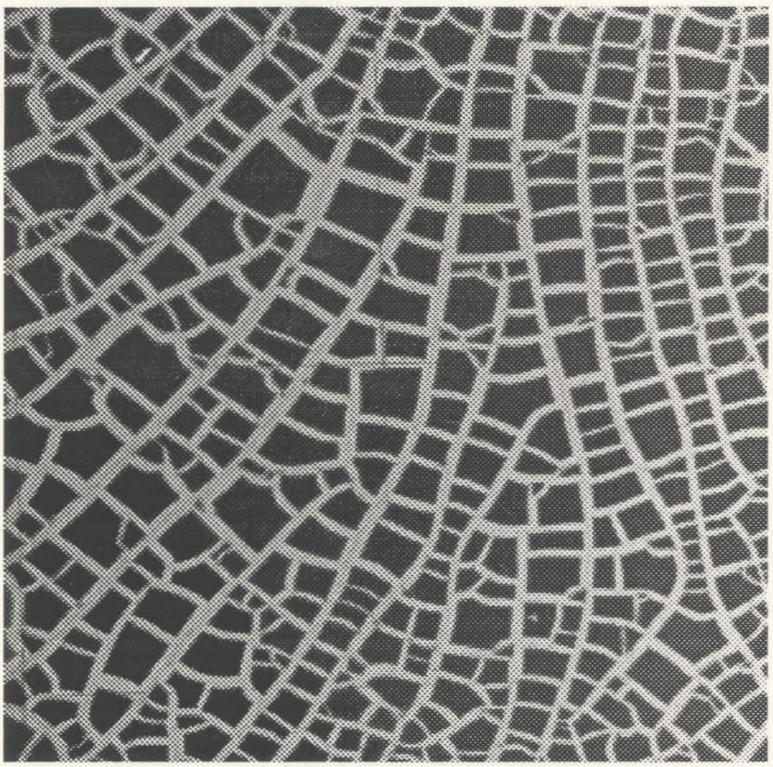

Figure 3.35: Pattern formed in a Type A experiment. $d = 2.27 \pm 0.20$ mm

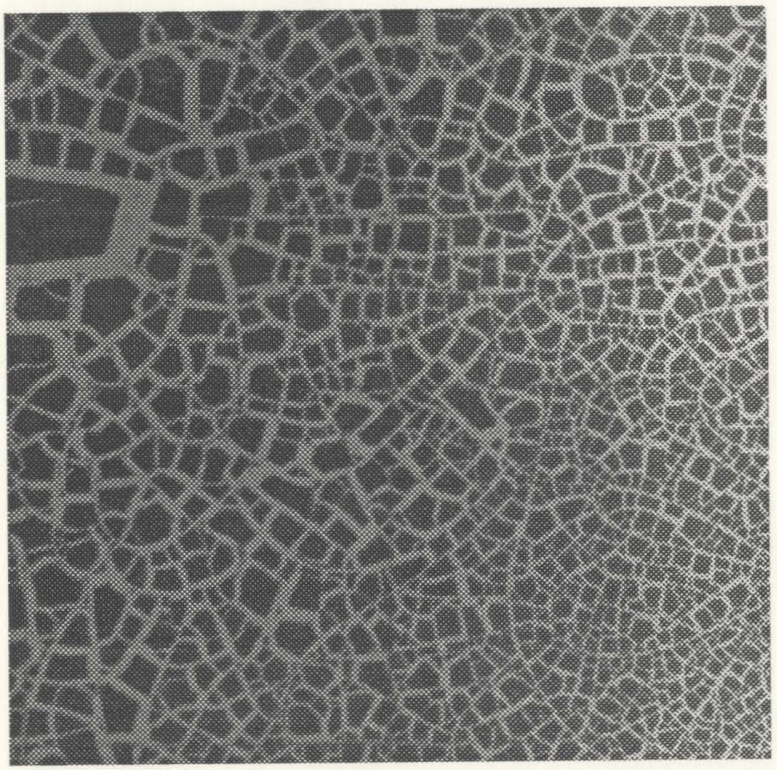

Figure 3.36: Pattern formed in a Type B experiment. $d = 0.83 \pm 0.18$ mm

Figure 3.37: Pattern formed in a Type B experiment. $d = 2.51 \pm 0.17$ mm

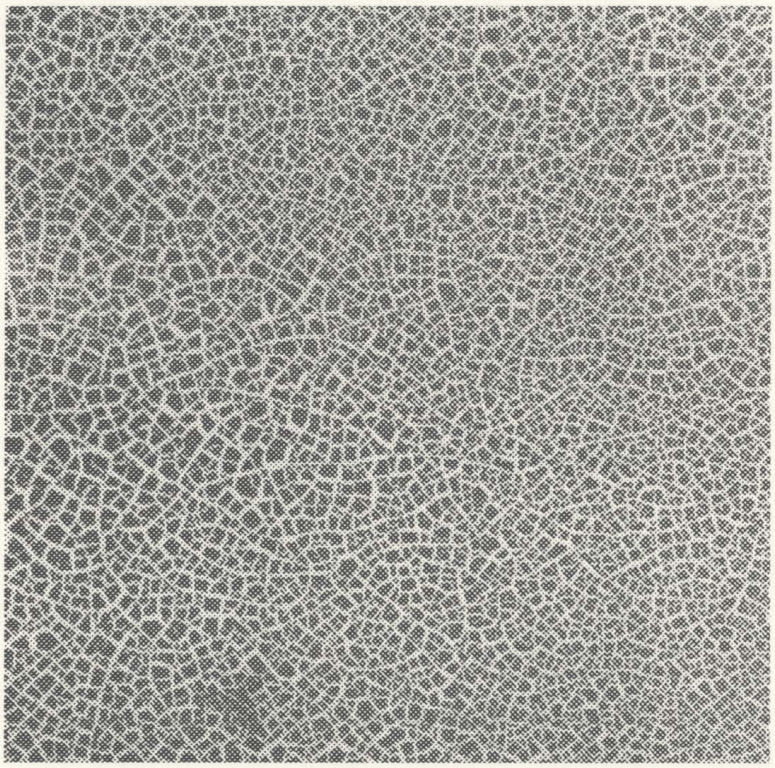

Figure 3.38: Pattern formed in a Type C experiment. $d = 0.60 \pm 0.03$ mm

3.6 Junction Angles as a Function of Depth

For several thicknesses in each different type of experiment, we measured the junction angles Θ between cracks. The junctions were measured on both sides of an intersection as shown in Fig. 3.39. The number of crack junctions in a given sample area depended on the thickness of the layer and ranged from 46 angles in the thickest layer to 513 in the thinnest layer. The error in measuring these angles was about 2° and the data were binned in 5° bins.

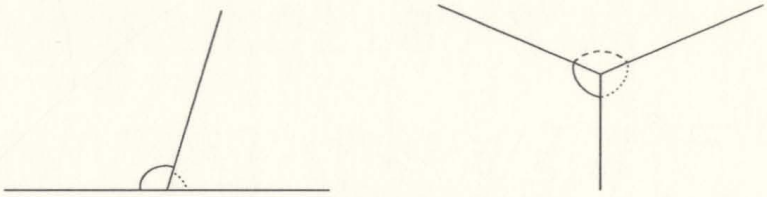

Figure 3.39: Location of junction angles measured.

The percentage of angles $P(\Theta)$ is plotted as a function of Θ in histograms in Figs. 3.40 – 3.43. In all cases the data have a strong central peak at 90° with scatter about the peak. The scatter in Type A experiments does not seem to change with depth. In Type B experiments, the scatter decreases with depth, except in the thickest layer. The histogram of these data, Fig. 3.42, has peaks at 35° and 145° . In this layer, there were only 46 junction angles, which is significantly fewer than in the other experiments (between 62 and 126 in the intermediate depth layers and 389 in the thinnest layer). Since the number of junctions in the sample area is low, these peaks are due to only two data points and may not be statistically significant. The histogram in

Fig. 3.43 shows that the distribution of angles is more narrow in the thicker layer of Type C experiments.

The mean and standard deviation of the distribution of angles were calculated by numerical integration. The mean of the data for all experiments is 90° within the experimental scatter. The standard deviation for each type of experiment as a function of depth is plotted in Fig. 3.44. The error in σ is taken to be 2.5°, half the bin width. The results shown in Fig. 3.44 are in agreement with the qualitative observations. σ is constant in Type A runs, it decreases in type B runs, except in the thickest layer, and appears to decrease in the Type C experiments.

In the previous section, the amount of scatter in the number of sides per polygon increased with depth for Types A and B experiments and stayed roughly the same in Type C experiments. The histograms in this section, Figs. 3.40 – 3.43, show that the scatter in the data stays approximately the same with depth in Type A runs and decreases with depth in the Type B and Type C runs. The decrease in the width of the distribution in Type B runs may be a result of more polygons with curved edges forming perpendicular junctions in polygons which are not 4 sided. In Type C experiments, the presence of the impurities may result in more non-perpendicular junctions in runs where the layer thickness is about the same as the size of the impurities which would give a wider distribution of junction angles in thinner layers.

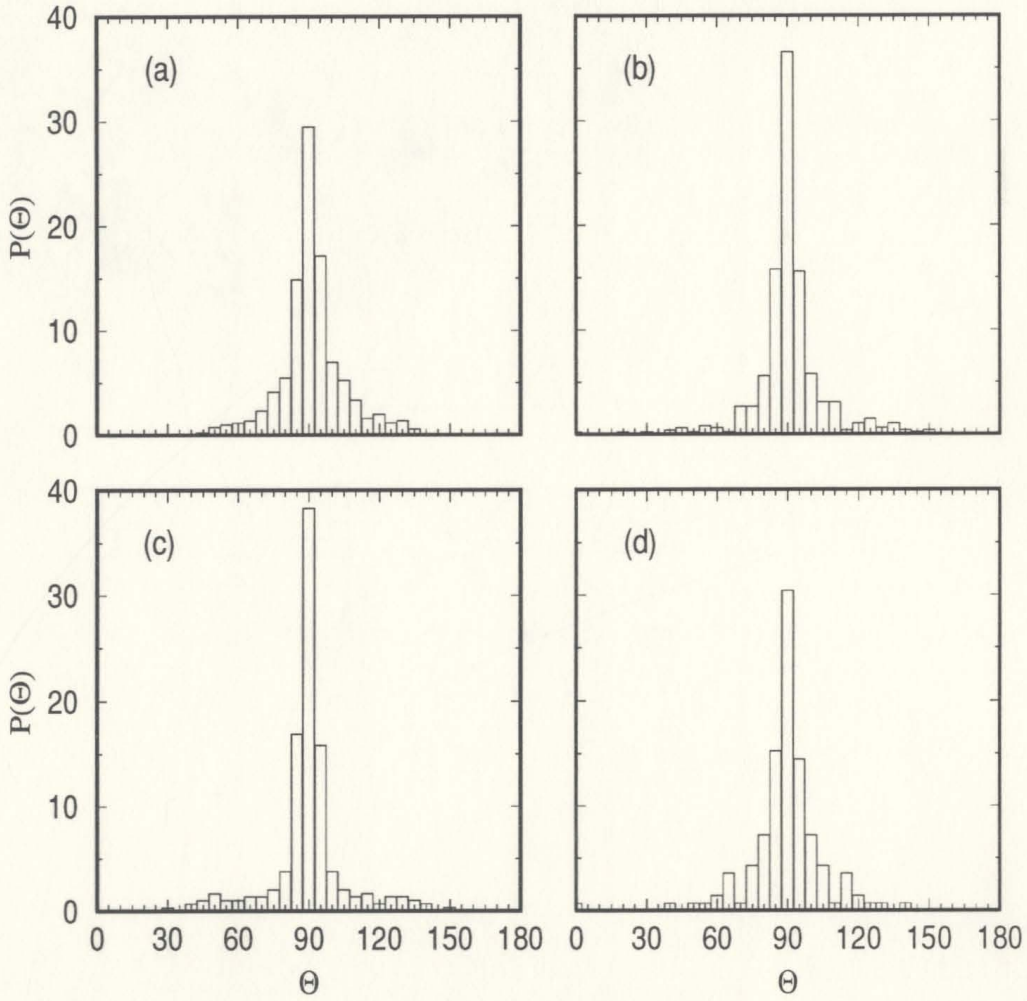

Figure 3.40: P(Θ) as a function of Θ of Type A experiments with (a) $d = 0.50 \pm 0.02$ mm, (b) $d = 1.78 \pm 0.03$ mm, (c) $d = 2.76 \pm 0.18$ mm, and (d) $d = 3.35 \pm 0.18$ mm.

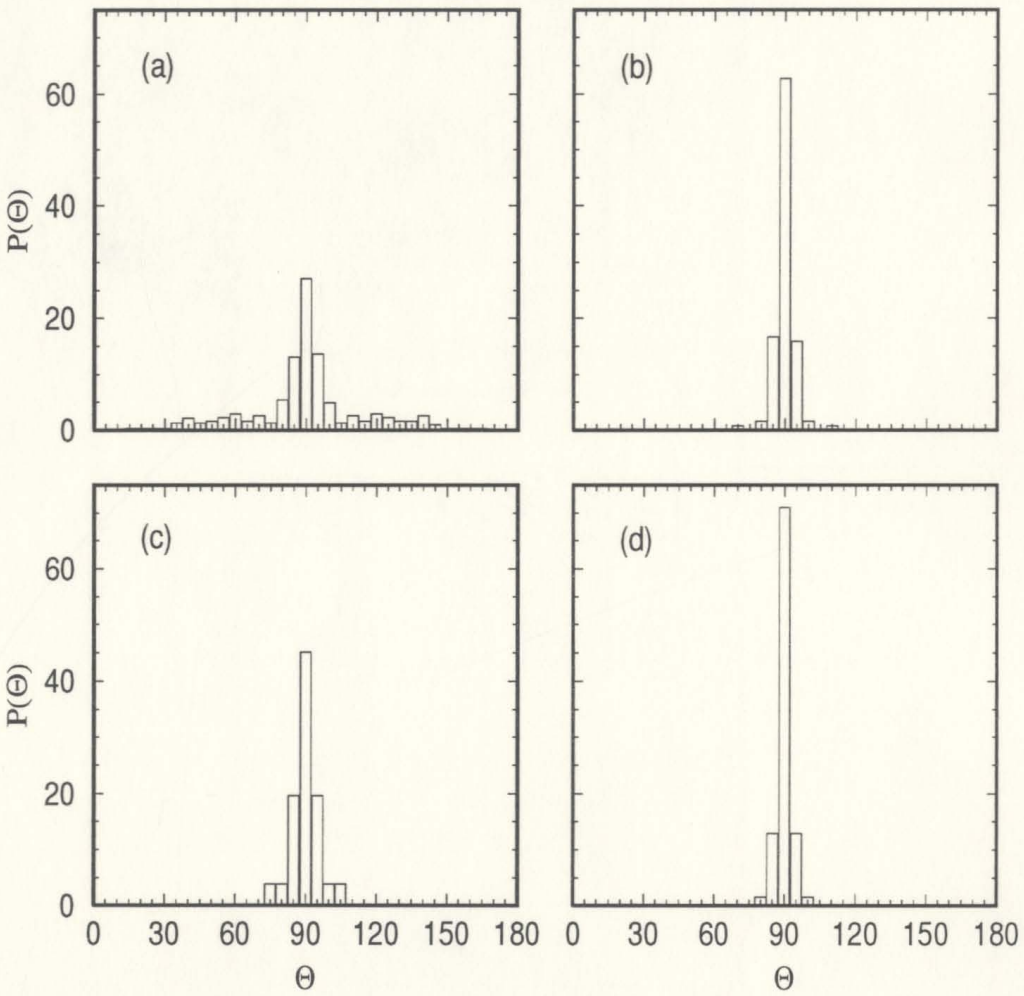

Figure 3.41: P(Θ) as a function of Θ of Type B experiments with (a) $d = 0.80 \pm 0.05$ mm, (b) $d = 2.20 \pm 0.04$ mm, (c) $d = 2.60 \pm 0.07$ mm, and (d) $d = 2.70 \pm 0.08$ mm.

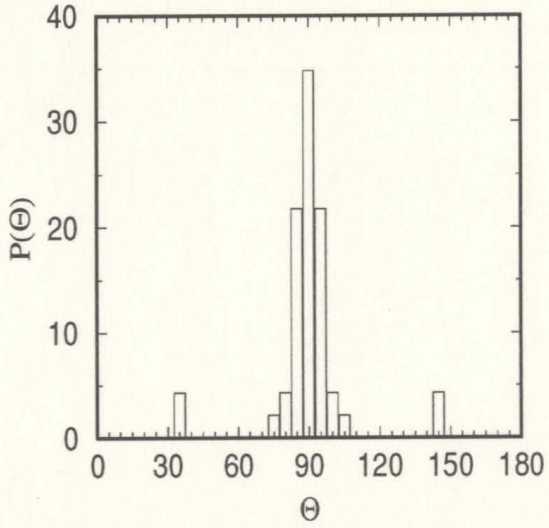

Figure 3.42: P(Θ) as a function of Θ of Type B experiment with $d = 3.27 \pm 0.30$ mm.

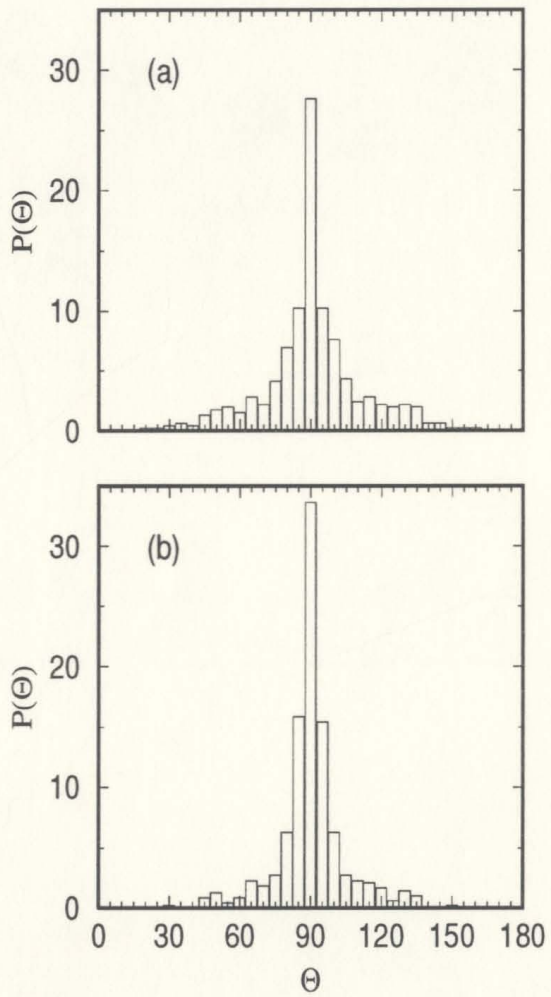

Figure 3.43: P(Θ) as a function of Θ of Type C experiments with (a) $d = 0.64 \pm 0.03$ mm and (b) $d = 2.13 \pm 0.06$ mm.

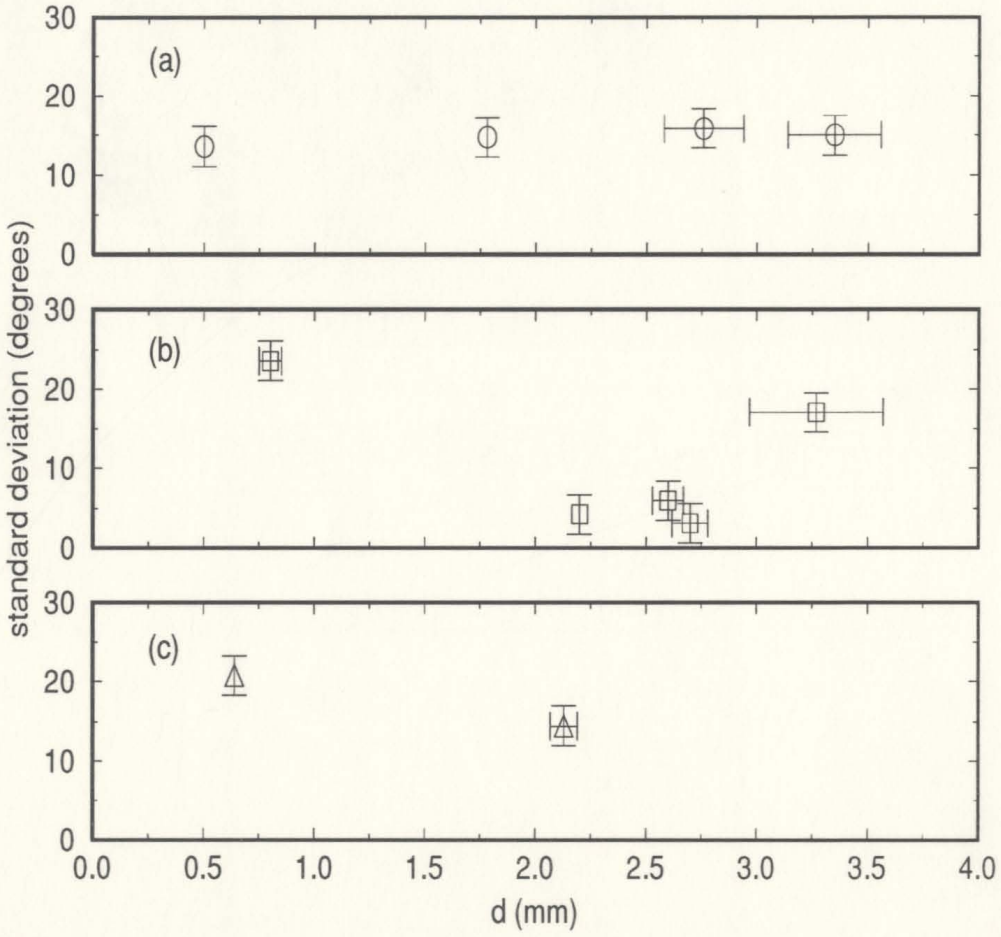

Figure 3.44: Standard deviation of the distribution of junction angles as a function of d for (a) Type A experiments, (b) Type B experiments, and (c) Type C experiments.

Chapter 4
Summary

We studied the shrinkage crack patterns that formed in a dried slurry of Al_2O_3 and water. The experimental parameters were the friction between the layer and its substrate, impurities added to the slurry, and layer thickness. To vary the parameters we did four individual runs for different layer thicknesses for each of three types of experiment. In Type A runs, the alumina had no added impurities and the substrate was untreated. The friction was reduced in the Type B runs by spraying the Plexiglas pan with a teflon coating and no impurities were added to the slurry. The Type C runs also had bottom friction reduced with a teflon coating, and impurities were introduced by sprinkling 10 cm^3 of sand grains evenly over the top of the slurry before the drying began.

We approximated the wavelength of the pattern by $\lambda \approx l/\sqrt{N_p}$ where N_p is the number of polygons in the sample area and l is the length of the sample side, by analysing images of the crack pattern. We found the wavelength to be proportional to depth for all experimental conditions. In the Type A runs, the slope was 3.60 ± 0.08. Under similar conditions, Groisman and Kaplan [7] observed a linear relation with a slope of about 0.4. This slope is smaller than our values but the grain size of the material used by Groisman and Kaplan is several orders of magnitudes larger than the grain size of the Al_2O_3 used in our experiments. Groisman and Kaplan qualitatively illustrated that reducing the friction between the layer and its substrate results in fewer

cracks in the layer. We studied this effect quantitatively by comparing the results of Type A and Type B experiments. The wavelength in Type B experiments was proportional to depth with a slope of 6.56± 0.26, which is larger than the slope for Type A experiments. This implies that stress builds up more slowly with distance away from an existing crack when friction is smaller, and indicates that bottom friction is the main source of stress for cracking. Type B experiments have a longer wavelength with fixed depth than Type C experiments, with a slope of 3.43± 0.04, which shows that adding impurities weakens the layer, causing more fractures.

We did two-dimensional fast Fourier transforms of the images captured from the video record of the cracks. From the azimuthally averaged power spectrum, we obtained information about the spatial structure of the pattern. The power spectra peaked about some wavenumber k_c. The lengthscale $1/k_c$ is another measure of the wavelength of the crack pattern, and this quantity was consistent with the wavelengths as found by counting polygons.

The moments μ_n of $P(k)$ about the mean wavenumber $\langle k \rangle$ were calculated by numerical integration and the values of standard deviation, skewness, and kurtosis were calculated with the μ_n. The standard deviation, or inverse of the correlation length, was constant with depth which shows that the lengthscale over which the pattern is correlated does not change with layer depth. In the experiments, $\xi \leq \lambda$ except in thin layers, so thicker patterns have little long range order. The standard deviations for Type A and Type B experiments were equal showing that changing the bottom friction did not

change the correlation length of the pattern. For Type C experiments, the standard deviation was larger indicating that the lengthscale over which the pattern was correlated became smaller.

For experiments without added impurities, the formation of a crack relieves stress locally. At some distance from the crack edge, depending on the stress distribution with thickness and the depth of the crack, the stress builds to its pre-cracking value and another fracture opens [2]. This leads to a lengthscale which is proportional to layer depth. However the spacing between individual cracks is probably influenced by three-dimensional effects in the stress relief zone, such as how the friction changes with layer depth, the influence of nearby cracks, and the stress distribution function with depth.

For experiments with added impurities, crack locations depend on this stress relief zone but are also influenced by the impurities. Cracks are nucleated more frequently at the nucleation sites provided by the impurities which are approximately randomly distributed in the bulk. Impurities may also cause crack tips to split during propagation or may change the direction of the crack motion during propagation, increasing the disorder of the pattern.

The skewness and kurtosis of the patterns increased with depth for all experiments. A skewness and kurtosis of zero would mean that the $kP(k)$ distribution was gaussian and the location of cracks would also have a gaussian distribution. The only run which had a near gaussian form was the thinnest layer of Type C experiment. In this run, the layer depth was 0.23 ± 0.02 mm

which is smaller than the impurity size of .425 – .500 mm, and the impurities had a greater effect in this run than in the other runs where the layer depth was thicker than the impurity size. Significantly more crack locations in this run were determined by the impurities, which were approximately randomly located. In the other experiments, the crack locations were more dependent on the stress relief zone.

An increased orientation of the pattern with depth of Type A and Type B runs is seen in Fig. 3.14 (d) and Fig. 3.15 (d) where the two-dimensional power spectra are anisotropic. Fig. 3.16 (d) is the power spectrum of a run of Type C of similar thickness and is more isotropic which implies less directional orientation in this run. The thinner layers of all experiments have more isotropic power spectra showing that the polygons in thinner layers are more randomly oriented.

For depths of from 0.5 mm to several millimetres we determined the percentage of polygons with n sides ($n = 3 \ldots 6$) for each of the different types of experiment. We found an increase in the percentage of 4 sided polygons and a decrease in the percentage of 3 sided polygons at a depth of about 1.5 mm in Type A and Type B experiments. This is a transition due to a change in the polygon formation at late stages of drying. After the initial pattern has formed, more water is lost through evaporation and the polygons contract further. In the thinner layers, the polygons tend to fragment as a result of stress caused by friction with the substrate. The fragments often split 4 sided polygons into pairs of 3 and 4 sided polygons or 3 and 5 sided

polygons. In thicker layers, the effects of friction are reduced and the stress is not large enough to cause the polygons to fracture. The transition was not observed in Type C runs because in these experiments, the impurities caused the fractures formed initially to be sufficiently close so that the strength of the smallest polygons exceeded the stress caused by further drying.

The analysis of the distribution of junction angles does not show a transition. The distribution of junction angles in all experiments was peaked at 90° with some scatter about the peak. In Type A runs, the scatter in the distribution of angles is approximately constant with depth. Neglecting the thickest point in the Type B runs, the distribution of junction angles becomes more narrow with increasing depth. In thicker runs of Type B, the cracks tend to curve, so that many of the 3 and 5 sided polygons are formed with cracks that meet at perpendicular junctions. The curving is not as apparent in Type A runs. The distribution also decreases with depth in Type C experiments. Type C experiments have more non-perpendicular junctions in thin layers because the size of the impurities is about the same as the layer depth and cracks are more easily nucleated at the impurities.

Groisman and Kaplan [7] noted a transition below 4 mm in their experiments which was marked by a change in the morphology to a pattern without a definite polygonal network and an increase in the percentage of 120° junction from close to 0 to about 30%. We did not see any such transition in our experiments. In all experiments, the patterns had a definite polygonal network with primarily perpendicular junctions and in all runs except

the thinnest layer of the Type C runs, all of the cracks were straight with smooth faces. The Al_2O_3 used in our experiments formed a very brittle layer when dry. Brittle fractures have high energy and are fast moving [5] and the crack opens before the surrounding stress field has time to completely relax to a new value. With slower moving cracks which form in less brittle substances, the stress field relaxes and changes as the crack propagates, making the crack path complicated. Smooth, polygonal crack patterns with perpendicular junctions, like the patterns we observe in the dried Al_2O_3 slurry, are typical of those formed by brittle fracture of the material. More diffuse patterns of cracks with a greater percentage of 120° crack junctions, like the patterns observed in the thin layers of Groisman and Kaplan's experiment, are also commonly observed in dried mud layers in nature, as in Fig. 1.1, pavement, and in layers of dried cornstarch and water mixtures [1]. A detailed study of the crack tip velocity and difference in the material properties of the substances which produce the different crack patterns would give more information.

In these experiments, we see linear relationships between lengthscale of the pattern and layer thickness. Bottom friction provides the main source of stress in fracture. The addition of impurities weakens a layer and results in a shorter lengthscale. With the Fourier analysis, we find the patterns have little long range order except in the thinnest layers, suggesting that three-dimensional effects are important. We see that in the thickest layers the pattern of polygons have increased spatial orientation. Most crack junctions

are perpendicular so they were formed primarily by crack intersections rather than nucleations or tip-bifurcations.

References

[1] Jearl Walker, *Scientific American* **255**, 284 (1986).

[2] Arthur H. Lachenbruch, *Geological Society of America Special Paper* **70** 1962.

[3] A. A. Griffith, *Philosophical Transactions of the Royal Society of London* Series A **221**,163 (1920).

[4] E. M. Kindle, *Journal of Geolology* **25**, 135 (1917).

[5] H. J. Herrmann and S. Roux, eds., *Statistical Models for the Fracture of Disordered Media* (North-Holland, Amsterdam) 1990.

[6] F. W. Christiansen, *Science* **139**, 607 (1963).

[7] A. Groisman and E. Kaplan, *Europhysics Letters* **25**, 415 (1994).

[8] J. Webb and T. Beddoe, unpublished.

[9] A. T. Skjeltorp and Paul Meakin, *Nature* **335**, 424 (1988).

[10] James T. Neal, *Geological Society of America Bulletin* **77**, 1327 (1966).

[11] J. Q. Tompkins, *Geological Society of America Bulletin* **77**, 1331 (1966).

[12] J. Q. Tompkins, *Geological Society of America Bulletin* **76**, 1075 (1965).

[13] T. Hornig, I. M. Sokolov, and A. Blumen, *Phsical Review E* **54**, 4293 (1996).

[14] K.-t. Leung and J. V. Andersen, preprint.

[15] J. V. Andersen *et al.*, *Europhysics Letters* **26**, 19 (1994).

[16] A. Yuse and M. Sano, *Nature* **362**, 329 (1993).

[17] M. Marder, *Nature* **362**, 295 (1993).

[18] C. Allain and L. Limat, *Physical Review Letters* **74**, 2981 (1995).

[19] T. S. Komatsu and S.-i. Sasa, *Japanese Journal of Applied Physics* **36**,391 (1997).

[20] S. Morris and M. Graham, unpublished.

Appendix A

The following code was written to do the Fourier analysis of the digitized images of the crack patterns with the software Matlab as outlined in Sec. 3.4.

```
%File last edited on February 24, 1997
%matlab code which reads in binary picture files of the shrinkage
%crack patterns and does a two dimensional fast fourier transform.

clear
format long;

%Read in  data

filename = input('Name of (binary) file to read: ','s');
rows     = input('rows (512): ');
columns  = input('columns (480): ');
fid = fopen(filename,'r');
a = fread(fid);
status = fclose(fid);

%The first 256 bytes are junk so we delete those.
%Put the column vector B into a matrix of appropriate dimensions.
%This is actually the transpose (due to the way meatlab reads a
%binary file) of what we want so we need to take the transpose of
%A and keep track of rows and columns.
```

```
B = a(257:(rows*columns+256));
A = reshape(B,rows,columns);
A = A';
temp = rows; rows = columns; columns = temp;

%clear the unecessary variables

clear a B temp;

%Taking the Power Spectrum of A will give a large peak at 0.  We're
%interested in the smaller peaks with lower intensity so to get this
%we subtract the average intensity of matrix A from each element.

mean_intensity = sum(sum(A))/(rows*columns);
B = A - mean_intensity;
clear mean_intensity A;

%B is a 'reduced' image.
%We take the 480x512 fast fourier transform of B.
%The fft is shifted (with the matlab function 'fftshift' so that the
%peak occurs in the centre, shifted by exchanging first and third
%quadrants and second and fourth quadrants.
%Then find the power spectrum of B to look at the peaks which should
```

```
%show a lengthscale of the pattern.

%With the software Transform we find the scale of the pixels.
%Input this data for scaling purposes of the final result.

row_scale = input('Row scale (n rows = 80.0 mm) n = ');
column_scale = input('Column scale (n columns = 80.0 mm) n = ');

b = fft2(B,rows,columns);
b_shift = fftshift(b);
Pbb = b.*conj(b)/(rows*columns);
Pbb_shift = b_shift.*conj(b_shift)/(rows*columns);

%plot the image and power spectra

X = 1:512;  Y = 1:480;

figure(1); clf; orient tall;
subplot(2,2,1);
imagesc(X,Y,B);
title('Image of Reduced Data File');
xlabel('xaxis (pixels)'); ylabel('yaxis (pixels)');
subplot(2,2,2);
```

```
imagesc(Pbb_shift);
title('Shifted Power Spectrum of Reduced Data File');
xlabel('xaxis (inverse pixels)');
ylabel('yaxis (inverse pixels)');
subplot(2,2,3);
imagesc(Pbb_shift(rows/2-3:rows/2+3,columns/2-3:columns/2+3));
title('(Part of)  Shifted Power Spectrum of Data');
xlabel('xaxis (inverse pixels))');
ylabel('yaxis (inverse pixels)');
subplot(2,2,4);
surf(Pbb_shift(rows/2-3:rows/2+3,columns/2-3:columns/2+3));
title('(Part of)  Shifted Power Spectrum of Data');
xlabel('xaxis (inverse pixels)');
ylabel('yaxis (inverse pixels)');
zlabel('intensity (arbitrary units)');
print -dps FIGURE1

%The shifted power spectrum has a large peak centred at zero with a
%smaller surrounding peak in a ring/elliptical shape.
%Now that we have the power spectrum we want to see where the peaks
%(maximum intensity) occur.
%We look at each point, calculate the distance (radius) from the
%centre, and plot intensity as a function of radius.
```

```
whos

%Find the centre of the pattern by looking at it

round(rows/2-3)
round(rows/2+3)
 round(columns/2-3)
round(columns/2+3)

row_centre = input('Centre row: ');
col_centre = input('Centre column: ');

figure(2);
imagesc(Pbb_shift(row_centre-60:row_centre+60,col_centre-68:col_centre+68));
axis('off');
print -dps FIGURE2

%The power spectrum is a function of wavevector k.
%The framegrabber used to obtain the image scales the image so that
%the units of kx = 0.8 X the units of ky.

%The power spectrum is a 480 X 512 matrix.
```

```
%We take the radial average inside of the matrix.
%The wavevector starts at the centre of the power sprectrum
%(row_centre, col_centre).
%The wavevector extends a length of only 240 elements so that it
%remain inside the matrix.

%n is the maximum wavector from the midpoint to the edge

n = 240;

%The first column of the vector 'intensity' must be scaled so that
%the maximum k vector is 0.5 (for critical sampling).

kmax = 0.5;

intensity = 0:1/(2*(n-1)):kmax;  %vector of length 240 elements
intensity = intensity';
intensity(:,2) = zeros(n,1);
count = zeros(n,1);

for r = 1:rows
for c = 1:columns
 ky = (r - row_centre)*kmax/n;
```

```
 kx = 1.25*(c - col_centre)*kmax/n;
 k = sqrt(kx^2 + ky^2);
 if k < (kmax - 1/(2*(n-1)))
  index = round(480*k);
  intensity(index+1,2)= intensity(index+1,2) + Pbb_shift(r,c);
  count(index+1) = count(index+1) + 1;
 end
end
end

intensity(:,2) = intensity(:,2)./count;
intensity(1:30,:)

MINIMUM = input('Index number of minimum radius: ');

figure(3); orient tall;
subplot(3,1,1);
plot(intensity(:,1),intensity(:,2));
title('Intensity vs Radius');
ylabel('intensity(:,2)');
xlabel('intensity(:,1)');
subplot(3,1,2);
plot(intensity(MINIMUM:n,1),intensity(MINIMUM:n,2));
```

```
ylabel('intensity(:,2)');
xlabel('intensity(:,1)');
subplot(3,1,3);
plot(intensity(:,1),log(intensity(:,2)));
xlabel('intensity(:,1)');
ylabel('log (intensity)');
print -dps FIGURE3

INTENSITY = intensity(MINIMUM:n,:);
save INTENSITY INTENSITY -ascii

upperlimit = n - MINIMUM;

%Numerically integrate the intensity

denominator = quad8('d_moment',0, upperlimit);
MEAN = quad8('n_mean',0,upperlimit)/denominator;
save MEAN MEAN -ascii;
for i = 0:4
exponent = i
save EXPONENT exponent -ascii
numerator(i+1) = quad8('n_moment',0,upperlimit);
moment(i+1,1) = i;
```

```
moment(i+1,2) = numerator(i+1)/denominator;
end

XI = 1/sqrt(moment(3,2)); %correlation length
S =  moment(4,2)*(moment(3,2)^(-3/2)); %Skewness
kappa = moment(5,2)*(moment(3,2)^(-2)) - 3; %Kurtosis

figure(4);clf;orient tall;
plot(INTENSITY(:,1),INTENSITY(:,1).*INTENSITY(:,2));
xlabel('wavevector k (inverse pixels)');
ylabel('k*intensity(k)')
print -dps FIGURE4;

POWER(:,1) = INTENSITY(:,1); POWER(:,2) = INTENSITY(:,1).*INTENSITY(:,2);
save POWER POWER -ascii

scaled_mean = MEAN*row_scale/80.0;
scaled_wavelength = 1/scaled_mean;
scaled_xi =   XI*80.0/row_scale;
scaled_inv_xi = 1/scaled_xi;

%Write results to a file.
outfile = input('Output filename: ','s');
```

```
fid = fopen(outfile,'a');
fprintf(fid,'\n\nResults from binary image %s\n',filename);
fprintf(fid,'File created on: %s in Matlab with angular.m\n', date);
fprintf(fid,'mean = %g (inverse pixels)\n',MEAN);
fprintf(fid,'correlation length = %g (pixels)\n',XI);
fprintf(fid,'skewness = %g (unit free)\n',S);
fprintf(fid,'excess kurtosis = %g (unit free)\n\n',kappa);
for i = 1:5
fprintf(fid,'Moment %g = %g\n',moment(i,1),moment(i,2));
end
fprintf(fid,'Input parameters\n');
fprintf(fid,'Scale of rows %g\n',row_scale);
fprintf(fid,'Scale of columns %g\n',column_scale);
fprintf(fid,'Centre row %g\n',row_centre);
fprintf(fid,'Centre column %g\n',col_centre);
fprintf(fid,'Minimum radius %g\n',MINIMUM);
fprintf(fid,'Scaled results: ');
fprintf(fid,'Mean (in inverse mm) = %g\n\t\t',scaled_mean);
fprintf(fid,'Mean^(-1) (wavelength) = %g\n\t\t',scaled_wavelength);
fprintf(fid,'Correlation Length (in mm) = %g\n\t\t',scaled_xi);
fprintf(fid,'Correlation Length^(-1) (in mm^-1) = %g\n',scaled_inv_xi);
fclose(fid);
```